LRP 455/92 May 1992

GLOBAL SAWTOOTH INSTABILITY MEASURED BY MAGNETIC COILS IN THE JET TOKAMAK

P.A. Duperrex, A. Pochelon, A. Edwards and
J. Snipes

This work was undertaken under Task
Agreement between the CRPP and JET
(CRPP TA/1)

accepted for publication in
NUCLEAR FUSION

GLOBAL SAWTOOTH INSTABILITY MEASURED BY MAGNETIC COILS IN THE JET TOKAMAK

P.A. Duperrex[1*], A. Pochelon[1], A. Edwards, J. Snipes[2].

JET Joint Undertaking
Abingdon, Oxfordshire OX14 3EA
Great Britain

ABSTRACT

This paper describes measurements of the sawtooth instability in JET, in which the instability wave function is shown to extend to the edge where it is measured using magnetic coils. The numerous magnetic probes in JET allow the time evolution of the (n=0, 1, 2, 3) toroidal Fourier components to be analysed. The n=1 magnetic component is similar to the m=1 soft X-ray centroid motion. This fact indicates the potential of edge signals in retrieving the poloidal mode spectrum of the q=m/n=1 surface. The spectrum evolution of the instability is compared for normal sawteeth (NST) and quasi-stabilised "monster" sawteeth (MST). The spectrum is slowly decreasing with n for NST and all the components belong to one ballooning-like deformation, whereas MST show a large n=1 kink-like motion with small and independent accompanying higher n modes. Important equilibrium changes occur already during the growth of the instability and the growth rate is much faster than exponential. Both these facts imply a non-linear nature of the instability growth. Parametric dependence of growthrates, amplitudes, toroidal spectrum shape, etc., are studied to characterize the NST and MST instabilies.

1) Permanent address: Centre de Recherches en Physique des Plasmas/EPFL, 21, Av. des Bains, CH-1007 Lausanne, Switzerland
2) Permanent address: MIT Plasma Fusion Center, 175 Albany St., Cambridge, MA 02139, USA
* Present address: Defence Technology and Procurement Agency, 65 Stauffacherstr. CH-3000 Bern 22, Switzerland

I INTRODUCTION

Although sawtooth instabilities have been observed in tokamaks and studied for many years [1], the understanding of their mechanism is still incomplete. A strong motivation for studying internal disruptions lies in the hope of stabilizing sawtooth relaxations in a reactor. The sawtooth duration has already been successfully extended to several global energy confinement times, thereby appreciably improving central parameters (JET's so-called monster sawteeth [2]) and typically doubling the fusion yield. A definitive understanding of the observed phenomena seems to lag behind experimental achievements. Among the reasons responsible for this situation is certainly the difficulty in measuring the central current profile with the required precision. Fast particle populations are also expected to play an important role [3,4]. Thus, the nature of the instability responsible for the sawtooth crash is not yet well known.

This paper aims to characterise the sawtooth instability or the succession of instabilities leading to the sawtooth crash (also called an internal disruption) using new, detailed experimental measurements from magnetic pick-up coils located in the shadow of the limiters. The paper concentrates on the rapid growth phase, a period which typically represents 0.1 to 1 percent of the full sawtooth period in JET. Although we use edge signals to measure internal disruptions, magnetic coils represent a powerful tool to characterize sawtooth instabilities in an elongated and tight-aspect-ratio machine such as JET. The numerous fast-sampled coils available in JET (18 poloidal at 8 symmetric toroidal locations), see Fig. 1, allow an efficient spatial and temporal description of the instability. This gives access to the toroidal mode number spectrum and its temporal evolution, the growth rates of the instability, etc.

The first sawtooth relaxation measurements, using soft X-ray emission [1], showed that the m=0, n=0 thermal relaxations were preceded by a growing m=n=1 helical perturbation localized at the estimated radius of the q=1 surface, and seen as a sinusoidal oscillation due to plasma rotation. The growth of this slow precursor oscillation was believed to be responsible for the sawtooth crash. However, its growth rate was an order of magnitude slower than the growth rate of the ideal internal kink mode [5]. Kadomtsev interpreted this precursor as an m=n=1 tearing mode growing to fully invade the core encompassed by the island [6]. This picture was in apparent contradiction with the observation of an m=n=1 oscillation continuing after the sawtooth crash [7]. The comparison of experimental soft X-ray traces with simulated chord signals obtained from model emission profiles, identified the slow oscillation as a growing, rotating island. This island could remain relatively small until the beginning of the fast sawtooth crash [8], which the simulation did not resolve. The rapidity of the sawtooth crash seemed to imply that the relaxation must involve an event faster than the island growth. The link between current profile and sawtooth activity was investigated by polarimetry measurements [9]. Fast changes in the central safety factor q(0) at the crash were shown by these diagnostics [9,10] and also by the use of global Alfvén waves [11]. The measured current and sawtooth crash times were comparable [11], indicating a non-diffusive, convective current transport mechanism.

The fast character of the sawtooth crash in large tokamaks such as JET [12] or TFTR was puzzling. Analytical calculations in toroidal geometry showed that the ideal internal kink was stable below a critical β_p [13]. Toroidal geometry couples the m=1 internal mode to outer resonant surfaces, thereby extending the motion to larger radii, an effect further enhanced by the inclusion of resistivity [14]. The addition of resistivity was shown to increase the growth rate over the ideal value [15]. Inclusion of electron inertia [16,17] further increased the growth rate to

the values observed in large and small tokamaks.

In JET, an edge magnetic perturbation correlated with the sawtooth crash was detected with the magnetic pick-up coils [18] and used to determine sawtooth characteristics [19,20]. Earlier hints of a direct effect of the sawtooth instability on the plasma edge were previously observed in the T-10 tokamak, where the liner exhibited arc tracks oriented along a direction corresponding to an m=1 n=1 mode, that is, oriented along q=1 [21]. The edge magnetic perturbation associated with the sawtooth crash is visible for all sawteeth in JET. In this paper, we make use of this edge magnetic perturbation to characterize different types of internal disruptions.

The paper is presented as follows. In section II, we characterize the magnetic perturbation occurring at the sawtooth crash and show how the toroidal mode number spectrum is obtained. With the help of soft X-ray data, we demonstrate in section III that edge magnetic measurements adequately represent the internal disruption, or sawtooth instability. In the following section IV, we discuss the significance of the toroidal mode number spectrum obtained and we compare spectra from normal sawteeth (NST) with those from stabilized or so-called "monster" sawteeth (MST). These data are used in section V to determine scaling laws for the internal disruption instability. The results are discussed in section VI and conclusions are presented in section VII.

II SPATIAL AND TEMPORAL CHARACTERISTICS OF THE GONG

The sawtooth instability is usually studied using core data such as the electron temperature or density, that is by following soft X-ray, electron cyclotron emission or interferometric measurements. In the JET

tokamak each sawtooth is accompanied by a marked poloidal magnetic field perturbation at the wall. When this magnetic perturbation was first observed [18,19], it was named the "gong perturbation", by analogy with a gong being hit in its centre by a hammer - the sawtooth instability - and thus being set into vibration out to the edge. It is interesting to note that magnetic activity equivalent to the gong had not been reported earlier in smaller machines. On the other hand, the fact that the gong can be easily observed on large machines with an aspect ratio similar to JET (R/a=2.5), such as TFTR (with R/a=2.9) [22] and DIII-D (with R/a=2.5) [23] suggests that mode coupling in tight aspect ratio tokamaks may be responsible for allowing the mode to be observed at the wall.

This chapter reports on measurements of the spatial properties of the sawtooth instability, using Fourier analysis of the edge magnetic perturbations in the toroidal and poloidal directions.

The gongs observed on the magnetic pick-up coils occur at the time of the temperature crash measured on the soft X-rays, Fig. 2. Their level is well above that of background oscillations and magnetic turbulence. The increase of the H_α signal, indicative of the heat pulse released by the internal disruption reaching the edge, starts some tens of milliseconds later. To avoid any possible instrumental timing lag, the different signals are recorded on the same ADC.

It must be noted from the beginning that this so-called gong activity is essentially different from Mirnov or island activity which is often modulated by the sawtooth activity, especially in low $q_\psi(a)$ discharges. Figure 3 shows an example of a gong taking place during Mirnov activity. In ohmic JET discharges, the gong typically develops in a tenth of a toroidal Mirnov rotation period. This already enables the two types of activity to be easily distinguished in the raw magnetic coil traces. In most JET ohmic discharges there are no slow oscillations (usually termed

precursor oscillations) before the sawtooth instability. The possible absence of any precursor was reported for earlier smaller tokamaks, especially for high density discharges [24,25].

The experimental set-up and typical discharge conditions used in the present study are now described. The $\tilde{b}_\theta$ probe layout is depicted in Fig. 1 for one of the eight equi-spaced octants. The pick-up coils have a 10 kHz high frequency cut-off (-3dB) imposed by a 2.5 mm thick protective inconel casing. However, signals can be measured up to 60 - 80 kHz [26]. The time scale of the oscillations studied here (50μs - 1ms) is therefore well covered by the measuring coils, but is short compared to the vacuum vessel penetration time (typically 4 ms for a transverse field [27]). The vessel is therefore nearly an ideal conductor for the time scales considered. The sampling rate of the acquisition was 40kHz, giving 25μs time resolution.

The sawteeth analyzed in this paper cover a large range of discharge conditions with major radius $R \cong 2.96$ m, minor radius $a = 1.25$ m, aspect ratio $2.4 < R/a < 2.6$, and plasma elongation $1.3 < b/a < 1.7$. The data were collected from ohmic and auxiliary heated discharges ($B\varphi < 3.4$T, $I_p < 6$MA) with a broad range of edge safety factors $2 < q_\psi(a) < 10$. The auxiliary heating was mainly Ion Cyclotron Resonance Heating (ICRH) ($P_{RF} < 10$MW) although some data with Neutral Beam Injection (NBI) ($P_{NBI} < 10$MW) or combined heating have also been included. With additional heating ohmic electron temperatures in the 2 - 4 KeV range could reach 8 KeV, increasing the sawtooth relative electron temperature drop $\Delta Te/Te$ from 10 - 20 % to 50 %. But more dramatically, the use of appropriate additional heating has allowed the sawtooth period to be prolonged from a few hundred milliseconds to several seconds. These "monster" sawteeth allow achievement of higher asymptotic central parameters and increased global confinement time [2]. Both normal sawteeth (NST) and monster sawteeth (MST) are analyzed in this paper.

Spatial characteristics of the gong are easily deduced by using the large number of $\tilde{b}_\theta$ pick-up coils available in JET. These coils, regularly distributed over the surface of the vessel, allow us to perform toroidal and poloidal mode number analysis, to measure in-out asymmetries and to deduce the helicity of the gong instability.

For the toroidal analysis, we use N=8 pick-up coils at the same poloidal location, but toroidally separated by 45°, allowing the n=0, 1, 2, 3 and cos(4ϕ) Fourier components to be measured. The standard measurements used the coils poloidally located on the low field side (LFS) due to their larger signals (usually coil 3, see Fig. 1), and also to avoid increased response delays due to additional in-vessel components in front of some more equatorial probes.

The cosine and sine components are defined as follows,
for the n=0 component:

$$c_{n=0} = \frac{1}{N} \sum_{i=1}^{N} \tilde{b}_\theta(\varphi_i)$$

$$s_{n=0} = 0$$

and for the higher n components :

$$c_{n>0} = \frac{2}{N} \sum_{i=1}^{N} \tilde{b}_\theta(\varphi_i) \cos(n\varphi_i)$$

$$s_{n>0} = \frac{2}{N} \sum_{i=1}^{N} \tilde{b}_\theta(\varphi_i) \sin(n\varphi_i)$$

where $\tilde{b}_\theta(\varphi_i)$ are the integrated pick-up coil signals at the toroidal angles $\varphi_i = i\frac{2\pi}{N}$. The modulus and the toroidal phase are then:

$$b_n = \sqrt{c_n^2 + s_n^2}$$

$$\phi_n = \arctan(s_n/c_n)$$

The following analysis uses integrated probe signals, unless otherwise specified. For the numerical integration yielding $\tilde{b}_\theta$, it was necessary to add a numerical first-order high-pass filter (time constant ≈ 3ms) to remove integration drifts, introducing a slight distortion of slow events. Thus, the contribution of occasional slow Mirnov oscillations is reduced, and the gong dynamic resolution is enhanced. This filtering explains the apparent slow decrease of the n=0 component following the sawtooth crash (see for example Fig. 4), which therefore remains essentially artificial.

The time dependence of the different n-components gives important information on the nature of the instability. As an example, the time evolution of the different components in the case of a normal sawtooth is shown in Fig. 4. The n=0, 1, 2, 3 (and cos(4 ϕ)) components are calculated from the 8 integrated coil signals. The time t_0 is arbitrarily defined as the time when the unintegrated n=1 component $\dot{b}_{\theta\, n=1}$ is maximum. The n=1 component typically develops in 100 to 500μs before reaching saturation. The n=1 component, in the range of a few 10^{-4}T for normal sawteeth, is clearly the dominant toroidal mode number, although the n=2 component is <u>not</u> negligible and typically represents 25% of the n=1 component at saturation. The spectrum shows a rapid decrease towards higher n's. This suggests that a toroidal mode number analysis of 8 coils should adequately describe the spectrum, if this trend continues at the higher n's. This has been verified by decreasing the number of coils used in the analysis from 8 to 4 coils, which changes the relative n=1 amplitude by only ~10^{-3}. This confirms that the motion is dominated by the n=1 component, and does not contain important n>2 contributions. The example in Fig. 5 shows that the n=1, 2, 3 components grow approximately in parallel (i.e. spectrum shape unchanged). At their

saturation the higher n's systematically exhibit a small lag (by a few tens of microseconds) as compared to the (n-1)th maxima. In other words, the spectrum shape spreads out at saturation.

The n=0 component corresponds to a global radial displacement towards the high field side, visible on the individual coil signals as a reduction of the 8 integrated $\tilde{b}_\theta$ signals. This n=0 motion, the Shafranov shift, starts at the same time as the other components, has maximum growth rate while the other components are saturating, and saturates whilst the n≥1 instability components vanish. The n=0 Shafranov shift occurs on the same time scale as the n≥1 sawtooth instability. This indicates that the $\beta_p + \frac{1}{2}l_i$ equilibrium change starts *at the beginning* of the instability growth, that is before the temperature collapse itself.

The poloidal mode number analysis is intrinsically more difficult because of the geometrical deformation of the poloidal coordinate system due to toroidicity. The toroidicity and the shape of the flux surfaces produce a distortion of the modes from pure Fourier components [28] and introduce coupling between Fourier components on different rational surfaces [14]. As a result, only overall behaviour like the dominant m number at the edge can be measured by a poloidal array of probes.

Figure 6 is an example of the type of poloidal analysis performed. The poloidal mode number is deduced from poloidal oscillation plots (number of poloidal oscillations) and is approximately $m \approx 2 = \text{int}(q_\psi(a))$ with $q_\psi(a) = 2.6$ (Fig. 6a). In addition, the two poloidal arrays, 180° toroidally apart, clearly demonstrate the dominant n=1 character. For an increased $q_\psi(a) = 4.2$ in Fig. 6b), the corresponding m-value also increases to about 4. These m-values are expected as a result of coupling between resonant surfaces. In general, the dominant m-number obtained by this means is of the order of q_ψ at the edge ($m \approx \text{int}(q_\psi(a))$ as in Fig. 6), though lower

values ($1<m<int(q_\psi(a))$ can also be transiently observed. This fact may be attributed to the details of the radial structure of the instability: in some cases modes resonant on an intermediate integer q surface may be stronger than the one at the edge, as far as their relative amplitudes at the probe location are concerned. Note that the observation is typical of the ballooning effect (also described as mode ballooning), occurring at small aspect ratio [29,30].

The gong shows some ballooning character in the form of an in-out asymmetry for limiter discharges, easily visible in the examples of Fig. 6, that is for discharges leaning on the LFS limiters. For these discharges, the gong appears to be stronger at the low field side (LFS) equator. This still holds when the discharge is leaning on the inner wall which produces a shorter plasma coil separation on the high field side (HFS) coils than on the LFS coils. Similar in-out asymmetry has also been observed for continuous m=2 Mirnov activity in JET [31].

The gong helicity sign, another characteristic quantity to trace back to the nature of the instability involved, can be deduced from two perpendicular arrays of magnetic probes either from the b_θ amplitude or from the poloidal and toroidal phase velocities. Measurements show that the gong helicity has the same sign as the equilibrium magnetic field.

The toroidal rotation of the instability can be measured using the results of the toroidal Fourier decomposition. The dominant component being n=1, its phase $\phi_{n=1}(t) = \arctan(s_{n=1}(t) / c_{n=1}(t))$ can thus be considered as the phase of the instability itself. In Fig. 7, a plot of two consecutive gongs of the same discharge is shown. The first indicates a nearly stationary toroidal perturbation whereas the second travels with a large phase velocity of the order of $1–5 \times 10^4$ m/s in the electron drift direction during the instability growth. The difference shown by these two

examples is very typical. This is also observed on the poloidal rotation measured by the pick-up coils or soft X-ray cameras (see Chap.III). This erratic behaviour indicates that the instability has no preferential direction and that details of the instability time evolution are not reproducible for two successive gongs. Thus, these rotation differences should be explained by fine details in the profiles that change from one sawtooth to the next.

III PLASMA DISPLACEMENT

As seen in the last section, the gong perturbation is detected at the same time as the sawtooth instability is observed on the soft X-ray signals. This synchronization indicates that the two perturbations are somehow linked or represent different observations of the same process. To demonstrate that the gong represents a direct measurement of the sawtooth instability, a parameter was found which could be measured independently by the soft X-rays and the magnetic pick-up coils. This parameter was the radial plasma displacement associated with the sawtooth instability. In this section, the edge displacement deduced from the magnetic gong signal is compared with the core motion measured from soft X-ray tomography.

The magnetic perturbation measured at the edge can be related to an edge motion, as in ideal MHD a magnetic perturbation is linked to a displacement by [32]:

$$\vec{\tilde{b}} = \vec{\nabla} \wedge (\vec{\xi} \wedge \overrightarrow{B_o}) \qquad (3.1)$$

Evidence of an edge perturbation during the sawtooth crash can also be found in Langmuir probe measurements (Fig. 8), where the ion

saturation current exhibits a signal similar to the magnetic signal at the time of the internal disruption. The radial edge displacement $\xi_r(a)$ can be estimated using the pick-up coil measurement of $\tilde{b}_\theta$. In the cylindrical approximation with a perfectly conducting plasma of radius a and a conducting wall of radius d, where the probes are also located, the radial displacement in front of the probe is found to be

$$\xi_r(a) = \frac{\tilde{b}_\theta(d)}{B_{\theta_o}(a)} \frac{d}{2m\left(1-\frac{nq}{m}\right)} \left[\left(\frac{d}{a}\right)^m - \left(\frac{a}{d}\right)^m\right] \tag{3.2}$$

where $B_{\theta_o}(a)$ is the equilibrium poloidal field [33].

This expression shows that the radial displacement $\xi_r(a)$ is directly proportional to the perturbed $\tilde{b}_\theta$ measured at the edge by a pick-up coil. Using the full set of toroidally distributed coils, the displacement can be decomposed into its toroidal Fourier components. Thus, the n'th mode displacement amplitude is:

$$\frac{\xi_{r_n}(a)}{d} = G_{mn} \frac{b_{\theta n}}{B_{\theta_o}(a)} \tag{3.3}$$

where $G_{mn} = \frac{1}{2m\left(1-\frac{nq}{m}\right)} \left[\left(\frac{d}{a}\right)^m - \left(\frac{a}{d}\right)^m\right] \cong 0.1$ is a geometrical factor

$b_{\theta n}$ = the n'th Fourier component of the magnetic perturbation.

The n'th mode displacement amplitude $\xi_{r_n}(a)$ is a non-local quantity resulting from Fourier analysis with the advantage of being invariant under toroidal plasma rotation. It therefore remains unaffected by plasma rotation.

The edge displacement measured from the magnetic field perturbation can be compared with the core displacement measured by

the soft X-ray diagnostic. In JET, two soft X-ray cameras, viewing the plasma from the top and the low-field-side midplane [34] allow the soft X-ray emission profile to be tomographically reconstructed. The soft X-ray signal response is limited by a high frequency 33 KHz 3dB cut-off. The m=1 radial plasma shift $\xi^{sx}_{m=1}$ in the centre can be calculated from the first moment of the soft X-ray emission, also called the centroid position [35]. The coordinates of the centroid are defined as follows

$$Z = \frac{\int z\, f(x,z)\, dx\, dz}{\int f(x,z)\, dx\, dz} \quad \text{and} \quad X = \frac{\int x\, f(x,z)\, dx\, dz}{\int f(x,z)\, dx\, dz} \tag{3.4}$$

where f(x,z) is the tomographically reconstructed soft X-ray emissivity; the integration can either be performed over the full profile or only over the region inside the sawtooth inversion radius. The centroid displacement is then

$$\xi^{sx}_{m=1} = \sqrt{(X-X')^2 + (Z-Z')^2} \tag{3.5}$$

the primed symbols referring to the position of the centroid before the instability growth.

In section II, the main component of the gong (magnetic) pulse was shown to be n=1. We therefore compare the amplitude of the n=1 gong mode with the m=1 centroid shift. Such a comparison is presented in Fig. 9 where the two displacements (Fig. 9a) are plotted on a logarithmic scale (Fig. 9b) to allow for an unknown multiplicative factor. Both displacements exhibit the same temporal behaviour and the two traces overlap almost exactly. The agreement is remarkable over the whole growth phase and for as long as the value of $b_{\theta n=1}$ is large. This already demonstrates that the gong is directly linked with the internal disruption instability. At maximum amplitude the magnetic signal is typically one order of magnitude larger than the background noise (i.e. typ. signal-to-noise ratio ≥ 10). A similar signal-to-noise ratio is obtained for the centroid measurement during ohmic sawteeth in quiescent discharges.

The limits of detectability are (0.5-1) $\times 10^{-4}$ T typically for the gong measurement, (corresponding to $b_{\theta n=1}/B_\theta(a) \approx 10^{-4}$) and 1mm for the centroid motion ($\xi^{sx}_{m=1}/r_{inv} \approx$ 1mm/0.5m $\approx 2 \times 10^{-3}$).

We now describe the growth, saturation and decay phases of the internal disruption instability. These phases are outlined in Fig. 9b) by the vertical dashed lines.

The fast rise of the instability commences some 250 ms before the central soft X-ray emission collapses (Fig. 9a). The fast growth lasts about 100 μs, until saturation of the motion occurs. During this period a growth rate of $\gamma = 1.6 \times 10^4$ s^{-1} is measured on the magnetic and soft X-ray diagnostics. Preceding this fast growth, a more extended phase of slow growth [35] is often detectable on the magnetic and soft X-ray diagnostics, provided the level of background mode activity is small (0.5×10^{-4} T and 1mm respectively). The presence of this first slow growth rate, smaller by more than one order of magnitude ($\gamma \cong 1.1 \times 10^3 s^{-1}$) on both diagnostics suggests two distinct growth phases. The initial period of slow growth can typically last one millisecond, whereas the second period of fast growth typically lasts 50-200 μs. Unless stated otherwise, the following growth rate analysis applies to the later fast growth phase. It must be noted that the sawtooth thermal collapse has hardly begun during the second rapid growth period.

The crash itself is only completed during the following saturation period, lasting typically 100 μs. After saturation, both motions decay and begin to diverge. This later discrepancy between the two displacements is not surprising and only appears when the $b_{\theta n=0}$ motion takes over from the $b_{\theta n=1}$ motion. The presence of the n=0 Shafranov shift is indeed sufficient to explain the observed discrepancy between $b_{\theta n=1}$ and $\xi^{sx}_{m=1}$ following the sawtooth collapse. While the $b_{\theta n=1}$ signal monitors a non-

local toroidal mode component, the centroid motion $\xi^{ex}_{m=1}$ on the other hand gives the total m=1 displacement in a specific poloidal plane. In fact, all n-components contribute to $\xi^{ex}_{m=1}$ (and not only the n=1 component), including the n=0 Shafranov shift which develops to a large amplitude in the late phase.

Thus, the two displacements have been demonstrated to be well correlated during the growth and saturation of the instability. An interesting corollary of this good agreement is the implicit demonstration that the soft X-rays represent an adequate monitor of the magnetic flux surfaces, at least during the growth of the instability.

The values of central and edge displacements are now compared. One should notice that the absolute value of the soft X-ray displacement depends on the extent of the integration domain used to calculate the centroid position. When the domain is restricted from the full profile (as in Fig. 9b) to the region within the inversion radius of the sawtooth (Fig. 9c), the calculated centroid displacement is typically increased from 3-4cm to 15cm, that is to about 1/3 of the inversion radius itself. The central motion is then better quantitatively represented when using the domain restriction, as noticed in [12]. In Fig. 9c) the motion of the maximum of the soft X-ray emission profile is also shown, which is moving close to the sawtooth inversion radius during the saturation phase.

The plasma edge displacement can be calculated from $b_{\theta n=1}$ by using relation (3.2) for the example in Fig. 9. The conditions are I_p=2.2MA, $B_{\theta_o}(a)$=0.27T, $T_{e(}0)$=7.1KeV, $\Delta T_e(0)$=2.8KeV, B_φ=2.1T, $q_\psi(a)$=4.75, m=int($q_\psi(a)$)=4. The magnetic signals for the toroidal mode analysis have been recorded with the coil nb. 3 (see Fig. 1 for the spatial configuration) with a≅1.4m and b≅1.64m. The maximum amplitude $b_{\theta n=1} \cong 1.5 \times 10^{-3}$T then corresponds to the radial displacement $\xi_{r\,n=1}(a) = 7 \times 10^{-4}$m. The

corresponding centroid shift value is $\xi^{sx}_{m=1} = 0.15$ m. The ratio of edge n=1 displacement to core displacement therefore yields: $\xi_{r\,n=1}(a) / \xi^{sx}_{m=1} \approx 5 \times 10^{-3}$ with $q_\psi(a) = 4.75$ and b/a=1.54. Such a small ratio emphasizes that the internal disruption instability, though observable at the edge, remains essentially an internal mode.

In the example of (Fig. 9), the time evolution of the toroidal phase is unperturbed by the growth of the instability, whereas in most cases it is possible to observe a sharp change at the beginning of the gong. This behaviour is dependent on the presence (or absence) of background Mirnov oscillations before the internal disruption. As mentioned above (see Fig. 7), the toroidal rotation of the instability exhibits erratic behaviour from sawtooth to sawtooth. However, measurements of the poloidal rotation direction given by the centroid motion (Fig. 9c) and the toroidal rotation given by the gong toroidal phase (Fig. 9a) can be combined to yield the mode helicity in an alternative way. This provides the same mode helicity as that obtained from the plasma edge using only the gong.

IV THE n-SPECTRUM OF NORMAL AND MONSTER SAWTEETH

In this chapter we extend the analysis of NST presented in chapter II to a comparative study of NST and MST spectra. As found in chapter III, the equivalence of the n = 1 gong component and the m = 1 centroid shift deduced from soft X-rays suggests that toroidal mode analysis performed at the edge can yield the full poloidal spectrum of modes on the q = 1 surface. This hypothesis is made as m/n = q on rational surfaces, and therefore m = n on the q = 1 surface; we make use of the fact that a toroidal mode number n is invariant in a torus (which will be developed shortly).

The measured toroidal component amplitudes decrease with n and the toroidal spectrum can be approximated by $b_{\theta n} = b_{\theta n=1}\, n^{-\alpha}$ (for n = 1, 2, 3) where α is the spectrum index. During the growth phase of the NST, this typically yields $1.5 < \alpha < 3$ as can be deduced for example from Fig. 5.

In the case of MST the spectrum is quite different. An example of a MST is shown in Fig. 10. This MST was obtained with an additional power of P ≈ 11MW of mixed RF (central resonance, D/H-minority) and NB heating (co-injection, injection angle ~17°). In this case the sawtooth duration τ_s has been extended from typically 0.1-0.2s to 1.47s, thus maintaining stationary T_e profiles over several confinement times. The evolution of the spectra during the growth phase at the end of a MST is quite different from that of the NST case. The n = 1 mode dominates the motion and is always more than an order of magnitude larger than the n = 2 component. The ratio $b_{\theta n=2}/b_{\theta n=1}$ for MST is in the few percent range. This result can be compared with NST (Fig. 5) where the $b_{\theta n=2}/b_{\theta n=1}$ ratio is much larger (typically 20-30%). The comparison between NST and MST spectra before saturation is well summarized by Fig. 11, where the ratio $b_{\theta n=2}/b_{\theta n=1}$ is shown as a function of the sawtooth period.

It is also interesting to notice that the MST n=1 mode grows faster than exponentially. The respective growth rates of the n=1, 2 and 3 components can differ (Fig. 10) and show roughly $\gamma_3 \approx \gamma_2 > \gamma_1$. This trend is not clearly marked for NST where the different modes can grow simultaneously (Fig. 5).

At full saturation of both NST and MST instabilities, the maxima of higher n components are increasingly time delayed relative to the n=1

component. For MST these delays are typically 30μs and 50μs for the n=2 and n=3 components respectively. These delays were shorter by a factor 3 for NST, yielding 10μs and 15μs respectively. The high level of modes remaining after the temperature crash in Fig. 10 is representative of most MST crashes.

Comparison of the n=1,2 and 3 toroidal phase velocities also gives information about the relation between the different n Fourier components. For both NST and MST, the n=1 toroidal phase sets in typically 1.5 ms before the crash. This represents the earliest sign of the instability detected by the magnetic coils; higher n phases appear somewhat later, due to a lower signal to noise ratio. In the case of NST (Fig. 12), the toroidal rotation frequency (i.e. toroidal phase time derivative $\dot{\phi} = \frac{d\phi}{dt}$) increases linearly (within ±30% error) with n:

$$(\dot{\phi}_{n=1}, \dot{\phi}_{n=2}, \dot{\phi}_{n=3}) = (1,2,3)\,\dot{\phi}_{n=1} \qquad \text{i.e.} \qquad \dot{\phi}_n = n\,\dot{\phi}_{n=1}$$

indicating that their phase velocities are similar:

$$v_n = \frac{\omega_n}{k_n} = \dot{\phi}_n \frac{R}{n} = \dot{\phi}_{n=1} R$$

Thus, the different n-modes can be essentially viewed as Fourier components of the same perturbation. When the n-modes grow in parallel, similar phase velocities indicate that the perturbation retains its basic shape during rotation and simply expands in size. When the growth rates are different, shape modification occurs. However, if the phase relation between the different n still holds, this must be simply interpreted as a shape change of the perturbation and must be differentiated from the simultaneous or delayed growth of independent n-modes. For MST the corresponding phase analysis is more difficult since the n=2 and n=3 modes emerge quite late above the noise level. When measurable, no simple relation between the different component phase velocities can be found. For instance, the n=3 component rotates in the

opposite direction in Fig. 10. This difference suggests that the n=1 instability may be accompanied by independent secondary n=2 or n=3 modes for MST conditions.

After the crash, locking of the n = 1, 2 and 3 modes to the tokamak vessel can occur for MST, as already noticed for the n = 1 locked-mode [36]. In this example (Fig. 10) mode locking occurs less than 100μs after the crash. This time is much shorter than the 4ms transverse field penetration time of the vessel [27]. Curiously enough, not all modes need lock together, as is the case for the n=3 component of Fig. 10 which continues to turn freely for 1.1ms before finally locking. For large MST, the n=1 mode locking can last until the end of the discharge, with negative effects on the confinement properties [36].

The validity of the edge measured n-spectra as a representation of the n-spectrum, and possibly the poloidal m-spectrum on the q=1 surface is an important consideration. On the q=1 surface the n-spectrum of the resonant modes is similar to the m-spectrum since we have m=n on this surface. Via toroidal coupling, perturbations are produced at intervening rational surfaces [14] and can then be observed at the edge (gong). Distortion of the central perturbation n-spectrum as measured at the edge can arise from several factors such as non-axisymmetry, multipolar field decay and non-linearity effects.

As far as non-axisymmetry is concerned, we have only retained gongs with vanishingly small preceding Mirnov oscillations, as these directly perturb the measurement. As a consequence, the most axisymmetric cases have deliberately been selected for this analysis.

Multipolar field decay attenuates the amplitude of higher n-modes in both vacuum and plasma, thereby artificially increasing the spectrum indices. This decay should affect NST and MST similarly, mainly affecting the spectrum shape, but not the evolution of an individual

component or the relative timing of several components.

We now discuss the non-linearity in the radial transfer function between the q=1 surface and the edge, though non-linearity is certainly most important in the q=1 region, where it may couple n's [37]. If non-linearity were important for the radial transfer function, an increased spreading out of the n-spectrum would be expected for the large perturbation of MST. On the contrary, a concentrated n=1 component is experimentally observed for large amplitude MST gongs. In addition, the comparison of NST and MST spectra taken at the same amplitude of $b_{\theta n=1} \approx 5\times10^{-4}$ T still shows this major difference in the two types of sawteeth spectra: this was carried out by comparing a NST spectrum just before saturation with a MST spectrum at an early stage of growth.

The distortion introduced by these effects should be numerically estimated for realistic equilibria and geometry, though such a study is outside the scope of this work. Nevertheless, the comparison between centroid motion and $b_{\theta n=1}$ (see chap. III) shows excellent agreement during the whole growth of the instability (irrespective of the mode amplitude). Thus, the distortion should be constant during the instability growth and not affect the interpretation of our results concerning differences in the characteristics of NST and MST spectra; it implies in particular that the source of the higher n's should mainly be in the center. In short, the measured spectra are indicative of a broad n-spectrum in the q=1 region for NST and of a sharp n=1 mode in the q=1 region q=1 for MST.

In summary, NST present a broader n-spectrum, the different n-components having similar growth rates and coupled phase velocities. On the contrary, MST exhibit a sharper n=1 signature, a faster than exponential growth and a seemingly random phase velocity relationship. These results indicate that equilibrium conditions for the sawtooth

instability are different for NST and MST. The duration of the whole saturation process, as measured by the delay separating n-component peaks, is several times longer for MST than for NST.

Translating these results in terms of the m-spectrum in the q=1 region, NST can be seen as a wide m bulging perturbation which rotates during the instability growth whilst retaining its shape (locked phase relation between n-components). On the other hand, MST can be seen as a sharp n=1 rotating perturbation, and therefore probably also m=1, accompanied by higher independent n-modes only just before the crash (no particular phase relation between n-components).

V n=1 AMPLITUDE AND GROWTH RATE PARAMETRIC STUDY

The perfect proportionality between gong amplitude and centroid shift allows the gong to be used to study the amplitude and growth rate γ of the internal disruption instability, and their dependence on plasma parameters, such as plasma current I_p, safety factor $q_\psi(a)$, central electron temperature $T_e(0)$, sawtooth period τ_s, etc.

a) Amplitude and growth rate calculations

The analysis of the amplitude and growth rate is performed by taking fast sampled data (40KHz sampling frequency during 200ms). For each gong the growth rate is calculated as follows, assuming an exponentially growing instability of the form:

$$\tilde{b}(x,t) = b_0 \mathrm{Re}\left[e^{i(\mathbf{k}\cdot\mathbf{x}-\phi_0(t))}\right] e^{\gamma t} \qquad (5.1)$$

where $\phi_0(t)$ is the phase due to mode rotation. The instability amplitude is $A(t) = b_0 e^{\gamma t}$ and an estimate of the growth rate γ can be obtained:

$$\gamma = \frac{dA(t)}{dt} A(t)^{-1} \qquad (5.2)$$

This expression is valid for any mode and therefore also for $b_{\theta n=1}$, the main component of the gong instability. Because of the time variation of the calculated growth rate, we use an averaged γ calculated around the time that the n=1 mode reaches half its peak amplitude, largely before any visible signs of saturation. It must be noticed that the time derivative of $b_{\theta n=1}$ is not equivalent to the n=1 component of the raw (unintegrated) data:

$$\frac{d}{dt}(b_{\theta n=1}) = \gamma b_{\theta n=1} \qquad (5.3)$$

whereas

$$\left(\frac{d}{dt} b_\theta\right)_{n=1} = (\gamma + i\frac{d}{dt}\phi(t))\ b_{\theta n=1} \qquad (5.4)$$

The extra term $i\frac{d}{dt}\phi(t)$ in (5.4) is due to the rotation of the mode itself.

The possible distortion of the measured growth rate due to the limited bandwidth of the measurements is now estimated. As previously mentioned, the inconel probe casing imposes a high frequency cut-off of 10 kHz (-3db). An numerical high-pass filter with a time constant of 3 ms was introduced to remove numerical integration drifts due to electronic drifts or background lower frequency Mirnov oscillations. Simulations show that the calculated growth rates are not significantly affected by this filtering or the 40kHz sampling rate in the range of the observed growth rates $1.5\times10^3 < \gamma < 9\times10^4\ s^{-1}$.

However, perturbative effects on the measurement of γ arise from the presence of underlying Mirnov activity. It has therefore been necessary for this study to select "quiescent" sawteeth that is without any marked precursor oscillations.

b) n = 1 mode amplitude

In the following, we first focus attention on NST, then compare the results with MST. The plasma currents (I_p) for the NST data base used in this chapter were 2, 2.8 and 4 MA, with a constant toroidal magnetic field of 3.4 T. Only ohmic shots or shots with very low ICRH power (P_{RF}<1MW) were used. The analysis shows that the amplitude of $b_{\theta n=1}$ reached at the end of the sawtooth crash, that is the value at saturation, is proportional to the amplitude of the electron temperature drop on axis $\Delta T_e/T_e$ (Fig. 13) for NST, when keeping the same main discharge parameters I_p, $q_\psi(a)$, and B_φ. A similar result is obtained when shown against $\Delta T_e(0)$. This again indicates a quantitative link between the edge magnetic perturbation and the amplitude of the central temperature or pressure perturbation for the same magnetic geometry.

MST show comparatively stronger gong perturbations: Fig. 14 shows $b_{\theta n=1}$ versus $\Delta T_e(0)/T_e(0)$ for some MST data. These values all sit above the NST extrapolation (lower left corner) by up to nearly an order of magnitude. An RF heated NST, taken out of the same MST shot series, is also shown in Fig. 14 as a reference. The shot parameters and the symbols used in this figure are summarised in Table I. The MST data in Fig. 14 cover wider experimental conditions (different $q_\psi(a)$, I_p, B_φ and P_{RF}) than the NST data in Fig. 13, thus a larger scatter is not surprising.

The observed gong amplitude is larger at low $q_\psi(a)$ and becomes almost undetectable at high $q_\psi(a)$. This trend can be seen even when normalised to plasma current to get a relative field perturbation (see Fig. 15, where NST are taken from only a narrow safety factor range: $5.0<q_\psi(a)<6.4$). The reduced amplitude observed at high $q_\psi(a)$ can be attributed to several experimentally inseparable factors. These are, as $q_\psi(a)$ increases, (i) the reduced volume encompassed by the q=1 surface,

(ii) the increased geometrical separation between the q=1 radius and the measuring coil, (iii) the increased number of resonance surfaces falling between the q=1 surface and the plasma edge, (iv) the likely larger m number of the gong for larger q, which produces a faster multipole roll-off.

The amplitude of $b_{\theta n=1}$, and therefore also the displacement $\xi^{sx}_{m=1}$ are linked to the sawtooth duration τ_s preceding the crash. For NST, this is shown in Fig. 16 where the amplitude increases statistically with sawtooth period τ_s. In addition, simple linear regression suggests that a minimum time of 50 ms (for the conditions in this series of shots) is needed to yield a non-zero signal. In other words, this is the minimum time (a dead time) needed after the crash to restore an equilibrium magnetic configuration which is again unstable with respect to an internal disruption. Unfortunately, since no sawteeth with periods less than 60 ms were observed on the central ECE electron temperature in this series, if we exclude very low density shots, we cannot rule out alternative functional forms such as τ_s^2 or exp (τ_s). For MST, (i.e. large τ_s), the $b_{\theta n=1}$ amplitude is much larger than for NST, as shown in Fig. 17, (shot parameters in Table I). As already noticed for the comparison between $b_{\theta n=1}$ and ΔT_e (see Fig. 14), the MST data exhibit a much larger scattering.

Previous sections have shown that $b_{\theta n=1} \sim \xi^{sx}_{m=1}$ during the instability growth and that $b_{\theta n=1} \sim \frac{\Delta T_e(0)}{T_e(0)}$ for NST. These relations demonstrate the central origin of the magnetic signal and suggest the combined scaling:

$$b_{\theta n=1} \sim \xi^{sx}_{m=1} \frac{\Delta T_e(0)}{T_e(0)} \tag{5.5}$$

which, by taking into account $b_{\theta n=1} \sim \tau_s$, valid only in a statistical sense

(Fig. 16), presents some analogy with the relation proposed by Wesson for NST [38] :

$$\tilde{b} \sim \xi_{instability} \frac{\Delta T_e(0)}{T_e(0)} \frac{\tau_S}{\tau_R} \quad (5.6)$$

where is the magnetic perturbation within the central region, τ_S is the sawtooth period and τ_R is the characteristic resistive diffusion time ($\tau_R = \frac{\mu_0}{4\eta} r_1^2$ with η the resistivity and $q_\psi(r_1)=1$).

c) Growth rates

Attempts to correlate the growth rate γ with macroscopic plasma parameters, using the same NST data base, were largely unsuccessful: see the large dispersion in Fig. 18 showing γ versus $b_{\theta n=1}$. To (further) illustrate this point, two consecutive NST gongs from the same discharge are presented in Fig. 19. The growth rate reaches $\gamma \approx 9 \times 10^3$ s^{-1} for the first gong and only $\gamma \approx 1.5 \times 10^3$ s^{-1} for the second one, although macroscopic conditions are identical. The growth rate can vary by almost one order of magnitude for two consecutive NST internal disruptions while discharge parameters such as I_p, $q_\psi(a)$, n_e, $T_e(0)$, β_p remain virtually unchanged. It is therefore not surprising that no precise scaling stems out of a parametric study of the NST growth rate.

Although the growth rates of NST show considerable scatter in Fig. 18, there is a statistical increase with the amplitude of the $b_{\theta n=1}$ gong perturbation measured at the edge. The same trend is also noticeable for MST, Fig. 20a), where growth rates in excess of 5×10^4 s^{-1} have been measured. The MST growth rates remain however a factor three below the linear extrapolation of NST (lower left corner in Fig. 20a). MST would therefore seem to obey a different scaling law, which is consistent with the observed $T_e(0)$ saturation for MST. Compared to Fig.20a), an apparently lower dispersion of the MST γ is observed when plotted against the sawtooth duration τ_S (Fig. 20b).

VI SUMMARY AND DISCUSSION

The analysis of the magnetic signals associated with the sawtooth instability has allowed us to characterise the different nature of NST and MST. An overview of the results is presented in Table II.

The proportionality between $\xi^{sk}_{m=1}$ and $b_{\theta n=1}$ (Fig. 9b) through q = m/n on the q = 1 surface has shown that the n = 1 mode wavefunction 1) is non-zero at the edge, and 2) that it reaches the edge without major deformation in time. These facts triggered a strong interest in following the higher n-components at the edge in their own right, and also as an alternative measurement of the m-components at q=1.

The NST instability is characterised by a slowly decreasing spectrum with the different n-components growing in parallel and with similar phase velocities ($v_{\phi\ n} \approx v_{\phi\ n=1}$). Thus, the n=1, 2 and 3 modes are not independent and must be viewed as Fourier components of a single bulging perturbation, which is typical of a ballooning type perturbation. The MST instability spectrum, on the contrary, is largely dominated by the n=1 mode, which grows independently of the other components, since there is no particular phase relation between the different n-components. The MST instability therefore shows the character of a kink motion.

The fact that NST and MST instabilities appear as essentially different spatial deformations suggests that different equilibrium conditions prevail in the two cases. The first major difference is the continuously decreasing central q(0) measured by polarimetry, as the sawtooth period increases, giving typically q(0) = 0.8 ± 0.15 for NST and q(0) = 0.7 ± 0.1 for MST [39,40], with larger Δq(0) excursions at each sawtooth crash [10]. Secondly, the pressure and temperature profiles are more peaked for MST, with high saturated central values ($T_e(0)$ = 5-9 keV, β_p= 0.35-0.50, for the examples of the figures), whereas for NST these values are still rising and sizeably lower (T_{eo} = 3-4keV, β_p = 0.10-0.15). The longer delay for MST between the component maxima at

saturation, several times longer than for the NST, could originate from the larger amount of flux to be rearranged in a MST instability crash, as polarimetry confirms [10]. Concerning the differences in spectra, resistive self-consistent equilibrium simulations show that large $\Delta q(0)$ excursions at the sawtooth crash correspond to narrower spectra, more concentrated on the n=1 mode [41]. Therefore the trend of the observed gong-spectra, taking into account the $\Delta q(0)$ excursions measured for NST and MST, fits well into this frame. The fast ion population, responsible for the increased stability of the m=1 component [3,4], may also affect the stability of the higher m-components.

The possible deformation of the n-spectrum as it couples to the plasma edge has been discussed in Chap. IV. It has been shown that if distortions exist, these do not question the difference between NST and MST n-spectra. Interactions between different m-components on the $q = 1$ surface may however occur. Toroidal and resistive effects can indeed superimpose higher (m,1) contributions onto the basic (m,n) = (1,1) component on $q = 1$ [14], however remaining at low level. This shows that the dominant mode on $q = 1$ is $m = n = 1$. This suggests that NST have a spread poloidal m-spectrum on the $q = 1$ surface whereas MST exhibit an almost pure $m = 1$ mode. To be strictly correct however, we will continue to speak about n-spectra rather than m-spectra on the $q = 1$ surface.

The instability growth rate for both NST and MST is not constant and tend to increase with τ_s. In many of the observed cases, it is possible to separate the growth into two distinct phases: a fast growing instability, generally preceded by a slow growing instability, which we will call the precursor instability. This slow instability can be measured at the edge ($b_{\theta n=1}$) or in the core ($\xi^{sx}_{m=1}$), and is seen in the Fig. 9b) for a NST and in Fig. 10 for a MST. The precursor growth rate is typically one order of magnitude smaller than the main growth rate (see summary Table II). It was not possible to perform a spectrum analysis of this slow precursor

instability, as the limited (low) signal to noise ratio only allowed the n=1 component to be measured faithfully. As a consequence, this paper only describes the main growth rate. As a whole, the sawtooth instability grows faster than exponential, which may imply that the instability consists of a succession of different instabilities. Experimental measurements of the displacement, where a two-step instability is often observed, would tend to substantiate this interpretation. Equilibrium changes may also explain this faster than exponential growth.

To consider the issue of equilibrium changes during the growth phase, let us use the information contained in the n = 0 gong component, which is the consequence of a $\beta_p + l_i/2$ decrease, and seen as a decrease of all $\tilde{b}_\theta$ traces measured with LFS coils (Fig. 4). The n = 0 traces (see for example Figs. 4, 10, and 19), show that the equilibrium begins to change during the growth of the instability. The maximum equilibrium rate of change occurs close to the n = 1 component maximum, which is also the position of maximum excursion of the soft X-ray centroid. Once the n = 1,2,3, ... components have saturated, the equilibrium freezes again. The fast equilibrium change that the plasma undergoes during the growth of the instability is an excellent candidate for explaining the non-constant growth rate measured. Therefore the evolution of both equilibrium and growth rates indicate non-linear phenomena.

The two main sequences in the instability growth rate (for both NST and MST) have suggested considering schemes with a sequence of instabilities, for instance two-step instabilities where a first instability, by modifying the equilibrium, induces a second instability, such as proposed by Bussac [42-44]. In such scenarios, an island can drive an ideal kink unstable [42,43], which in turn can drive ballooning modes unstable [44], or a resistive m=n=1 kink develops slowly into a saturated state which suddenly releases the energy in a fast growing kink [45]. Simulations with resistive, self-consistent equilibrium evolution reproduce well many features of the sawtooth activity in small and medium size tokamaks [41],

but cannot yet be used to compute sawtooth activity in large tokamaks, due to excessively large Lundquist number.

The growth rate changes by almost one order of magnitude for identical global conditions, such as in the case of two successive NST, and must therefore depend on local profile values, such as q(r) or $\beta_p(r)$. Pellet ablation measurements in NST [46] indicate a rather low shear of q(r) around the q=1 surface. Small changes in $\nabla q(r)$ at the q=1 surface in Textor [9] are shown to influence the stability of the m=1 mode.

Although MST statistics are limited, it seems that MST show a more predictable growth rate (Fig. 20a) compared to NST (Fig. 18). This may originate from steeper gradients $\nabla q(r)$ at the q=1 surface, or possibly from the simpler nature of the MST instability, made practically of only one independent n=1 kink mode.

Although two successive sawteeth can have very different growth rates, this does not seem to influence the spectrum shape in the example of Fig. 19, apart from a factor $\Delta T_e/T_e$ which multiplies all the components.

VII CONCLUSION

The sawtooth instability, that is the instability terminating the sawtooth oscillation, has been studied by measuring its wavefunction using edge magnetic probes.

The knowledge of the n- or m-spectrum on the q=1 surface is important for understanding the sawtooth instability in tokamaks. Soft X-ray camera measurements imply the use of tomographic reconstructions for which the capability to resolve high m's depends on the number of cameras used and requires a large number of signals to be treated. The use of an array of only eight magnetic b_θ-probes yields the n=0,1,2,3 toroidal spectrum components and reveals the detailed time evolution of

these n-components, and by association the m-components on q=1. A major advantage of magnetic data processing is that it only involves simple Fourier decomposition, does not depend on plasma rotation and requires no model assumption.

The similarity in time of the n=1 magnetic perturbation and the m=1 displacement of the central flux surfaces demonstrates the potential of edge magnetic measurements to determine the wavefunction of the instability on the q=1 surface. The different nature of NST and MST has been firmly established. From the geometry of the perturbation, NST exhibit a ballooning-like character, whilst MST exhibit a n=1 (kink-like)-motion. Non-linearity has to be invoked both in order to describe the faster than exponential growth and because equilibrium changes occur during the growth of the instability.

Acknowledgements

We would like to acknowledge B. de Kock and G. Tonetti for making the magnetic diagnostics available. We would also like to acknowledge discussions with M.N. Bussac, R. Granetz, F. Troyon and A. Turnbull. It is a pleasure to recall here the many stimulating discussions with A. Bondeson and we are indebted for his helpful comments. We are grateful to M. Dutch for his help in improving the manuscript. We also acknowledge the support of P.E. Stott and F. Troyon. We would like to thank the JET staff, in particular the RF-Heating team, the ECE and Plasma Boundary Groups for experimental support. This work was undertaken under Task Agreement between CRPP and JET (CRPP TA/1) and was partly supported by the Swiss National Science Foundation.

REFERENCES

[1] VON GOELER, S., STODIEK, W., SAUTHOFF, N., Phys. Rev. Lett. 33 (1974) 1201.

[2] CAMPBELL, D.J., START, D.F.H., WESSON J.A. et al., Phys. Rev. Lett. 60 (1988) 2148.

[3] WHITE, R.B., RUTHERFORD, P.H., COLESTOCK, P. and BUSSAC, M.N., Phys. Rev. Lett. 60 (1988) 2038.

[4] COPPI, B., HASTIE, R.J., MIGLIULIO, S., PEGORARO, F., PORCELLI, F., Phys. Lett., 132A (1988) 267.

[5] ROSENBLUTH, N.M., DAGAZIAN, R.Y., RUTHERFORD, P.H., Phys. Fluids 16 (1973) 1894.

[6] KADOMTSEV, B.B., Fiz. Plazmy 1 (1975) 710; Sov. J. Plasma Phys. 1 (1975) 389.

[7] EQUIPE TFR, 6th Int. Conf. on Plasma Phys. and Contr. Nucl. Fus. Res., IAEA, Berchtesgaden 1976, Vol. I, (1977) 279.

[8] DUBOIS, M.A., MARTY, D.A., POCHELON, A., Nucl. Fus. 20 (1980) 1355.

[9] SOLTWISCH, H., STODIEK, W., MANICKAM. J., SCHLUTER, J., 11th Int. Conf. on Plasma Phys. and Contr. Nucl. Fus. Res., IAEA, Kyoto 1986, Vol. I, (1987) 263.

[10] O'ROURKE, J., Plasma Phys. Contr. Fusion 33 (1991) 289.

[11] DE CHAMBRIER, A., DUPERREX, P.A., HEYM, A., HOFMANN, F., JOYE, B., KELLER, R., LIETTI, A., LISTER, J.B., POCHELON, A., SIMM, W., Phys. Lett. 92A (1982) 279.

[12] EDWARDS, A.W., CAMPBELL, D.J., ENGELHARDT, W.W., FAHRBACH, H.U., GILL, R.D., GRANETZ, R.S., TSUJI, S., TUBBING, B.J., WELLER, A., WESSON, J.A., ZASCHE, D., Phys. Rev. Lett 57 (1986) 210.

[13] BUSSAC, M.N., PELLAT, R., EDERY, D., SOULE, J.L., Phys. Rev. Lett. 35 (1975) 1638.

[14] BUSSAC, M.N., EDERY, D., PELLAT, R., SOULE, J.L. 6th Int. Conf. on Plasma Phys. and Contr. Nucl. Fus. Res., IAEA, Berchtesgaden 1976, Vol. I, (1977) 607.

[15] COPPI, B., GALVÃO, R., PELLAT, R., ROSENBLUTH, M., RUTHERFORD, P., Fiz. Plazmy 2 (1976) 961, Sov. J. Plasma Phys. 2 (1976) 533.

[16] WESSON, J.A., Nucl. Fus. 30 (1990) 2545.

[17] DRAKE, J.F., KLEVA, R.G., Phys. Rev. Lett. 66 (1991) 1458.

[18] DUPERREX, P.A., KELLER, R., POCHELON, A., TONETTI, G., Helvetica Physica Acta 58 (1985) 85.

[19] DUPERREX, P.A., KELLER, R., MALACARNE, M., POCHELON, A., 12th EPS Conf. on Contr. Fusion and Plasma Physics, Budapest, Edit.: EPS, Geneva.Vol. 9F, Part I (1985) 126.

[20] DUPERREX, P.A., POCHELON, A., EDWARDS, A., GRANETZ, R., SNIPES, J., 15th EPS Conf. on Contr. Fusion and Plasma Heating, Dubrovnik, Vol. 12B, Part I (1988) 362.

[21] ALEXANDER, K.F., HINTZE, W., LAUX, M., PECH, P., WOLFF, H., CHICHEROV, V.M., Nucl. Fus. 24 (1984) 631.

[22] McGUIRE, K.M., ARUNASALAM, V.,BELL, M.G., et al., 11th. Int. Conf. on Plasma Phys. and Contr. Nucl. Fusion Res., IAEA, Kyoto 1986.Vol. I, (1987) 421; McGUIRE, K.M. et al., Plasma Phys. and Contr. Nucl. Fusion, 30 (1988) 1391.

[23] STRAIT, T., GA Technologies, San Diego, California, U.S.A., personal communication (1987); and SIMONEN, T.C., et al., Phys. Rev. Lett. 61 (1988) 1720, Fig. 3d).

[24] TFR group, Association Euratom-CEA, Fontenay-aux-Roses, France, personal communication (1978).

[25] SNIPES, J.A., GENTLE, K.W., Nucl. Fus. 26 (1986) 1507.

[26] MALACARNE, M., DUPERREX, P.A., Nucl. Fusion 27 (1987) 2113.

[27] CORE, W.G., NOLL, P., Transverse magnetic field penetration through the JET toroidal coil and support structure, JET Report JET-R (88) 03 (1988).

[28] MEREZHKIN, V.G., Sov. J. Plasma Phys. 4 (1978) 152.

[29] TROYON, F., Course and Workshop on Basic Physical Processes of

Toroidal Plasmas, Varenna (1985), Commission of the European Communities and Monotypia Franchi Città di Castello (PG) Italy, Vol. I (1985) 259.

[30] TURNBULL, A.D., TROYON, F., Nucl. Fus. 29 (1989) 1887.

[31] HENDER, T.C., ROBINSON, D.C., SNIPES, J.A., Plasma Phys. and Contr. Nucl. Fusion Res., Proc. 11th Conf., Kyoto, IAEA, Nucl. Fusion, Suppl. 1987, Vol. I (1986) 291.

[32] BATEMAN, G., MHD Instabilities, The MIT Press, Cambridge, Mass. (1978)

[33] POCHELON, A., KELLER, R., J. Plasma Physics 16 (1976) 363, and references therein.

[34] EDWARDS, A.W., FAHRBACH, H.-U., GILL, R.D., GRANETZ, R.S., OORD, E., SHRAMM, G., TSUJI S., WELLER, A., ZASCHE, D., Rev. Sci. Instrum. 57 (1986) 2142.

[35] GRANETZ, R.S., EDWARDS, A.W., GILL, R.D., WELLER, A., 14th EPS Conf. on Contr. Fusion and Plasma Physics, Madrid, Vol. 11D, Part III (1987) 1256.

[36] SNIPES, J.A., CAMPBELL, D.J., HAYNES P.S., HENDER, T.C., HUGON, M., LOMAS, P.J., LOPES CARDOZO, N.J., NAVE, M.F.F., SCHÜLLER, F.C., Nucl. Fusion 28 (1988) 1085.

[37] BONDESON, A., Centre de Recherches en Physique des Plasmas / EPFL, Association Euratom-Confédération Suisse, Lausanne, Switzerland, personal communication (1991).

[38] WESSON, J.A., JET Joint Undertaking, CEC, Abingdon, Oxfordshire, U.K., personal communication (1987).

[39] O'ROURKE, J., BLUM, J., CORDEY, J. G., EDWARDS, A., GOTTARDI, N., KEEGAN, B., LAZZARO, E., MAGYAR, G., STEPHAN, Y., STUBBERFIELD, P., VERON, D., ZASCHE, D., 15th EPS Conf. on Contr. Fusion and Plasma Heating, Dubrovnik, Vol. 12B, Part I (1988) 155.

[40] CAMPBELL, D.J., CORDEY, J.G., EDWARDS, A.W., et al., 12th Int. Conf. on Plasma Physics and Contr. Nucl. Fusion Res., IAEA, Nice 1988, Vol. I (1989) 377.

[41] VLAD, G., BONDESON, A., Nucl.Fus. 29 (1989) 1139.

[42] BUSSAC, M.N., PELLAT, R., SOULE, J.L. and TAGGER, M., Phys. Lett. 105A (1984) 51 ; and Phys. Lett. 109A (1985) 331.

[43] BUSSAC, M.N., LEHRBINGER, K., PELLAT, R., TAGGER, M., 11th. Int. Conf. on Plasma Phys. and Contr. Nucl. Fusion Res., IAEA, Kyoto 1986, Vol II (1987) 17.

[44] BUSSAC, M.N., PELLAT, R., Phys. Rev. Lett. 59 (1987) 2650.

[45] SATO, T., NAKAYAMA, Y., HAYASHI, T., WATANABE, K., HORIUCHI, R., Phys. Rev. Lett. 63 (1989) 528.

[46] PEGOURIE, B., DUBOIS, M.A., Nucl. Fus. 29 (1989) 745, and GILL, R.D., EDWARDS, A.W, WELLER, A., Nucl. Fus. 29 (1989) 821

Table I. Shot parameters for MST data (for Figs. 14, 17, 20a and b)

	13412-20	19735-62	16052, 16448
B_φ (T)	2.8	3.0	3.0, 3.1
I_p (MA)	3.0-3.3	3.0-3.2	2.9
$q_\psi(a)$	4.3-5.8	3.0-3.2	3.7
b/a	1.54	1.4	1.4
P_{RF} (MW)	~8.	5.-9.	8., 3.
ICRH-scheme	D/H (12-14)	D/H (35-52)	D/H
	He^3/H (15-20)	He^4/H (54-62)	
	(Majority/Min.)		
P_{NBI} (MW)	0.	0.-10.	4., 5.5
	■ MST	● MST	Δ ∇ MST
	□ heated NST	L ● LFS heated MST (3.3T)	
	∇partial ST	H ● HFS heated MST (2.85T)	

Table II.

	NST	**MST**
Amplitudes:	$b_{\theta\, n=1} < 4 \times 10^{-4}$ Tesla	$3 < b_{\theta\, n=1} < 8 \times 10^{-3}$ Tesla
Growth rates:		
precursor instab.	$\gamma \sim 10^3\ s^{-1}$	$\gamma \approx (4\text{-}5) \times 10^3\ s^{-1}$
main instability	$\gamma \leq 2 \times 10^4\ s^{-1}$ $\tau = 50\text{-}400\mu s$ (large dispersion)	$3 \leq \gamma \leq 9 \times 10^4\ s^{-1}$ $\tau = 10\text{-}30\mu s$
Spectra:		
analysed modes	n = 0,1,2,3,cos(4ϕ)	n = 0,1,2,3,cos(4ϕ)
$b_{\theta\, n=2}/b_{\theta\, n=1}$ ratio	0.15 - 0.36	0.03 - 0.06
Saturation delay between successive modes $\tau^{sat}_{1\text{-}2}$ and $\tau^{sat}_{2\text{-}3}$	$\tau^{sat}_{1\text{-}2} \sim 10\ \mu s$ $\tau^{sat}_{2\text{-}3} \sim 15\ \mu s$	$\tau^{sat}_{1\text{-}2} \sim 30\ \mu s$ $\tau^{sat}_{2\text{-}3} \sim 50\ \mu s$
Phase and phase velocity	$(\dot{\phi}_{n=1}, \dot{\phi}_{n=2}, \dot{\phi}_{n=3}) \approx (1,2,3)\, \dot{\phi}_{n=1}$ i.e. $v_{\phi\ n} \approx v_{\phi\ n=1}$	no characteristic phase relation observed between the n=1,2,3 modes
safety factor q(0)	0.8 ± 0.15 [40]	0.7 ± 0.1 [40]
poloidal beta: β_p	0.10 - 0.15	0.35 - 0.50
$T_e(0)$	2.8 - 3.8 KeV	5 - 9 KeV steep gradients inside q=1 with enlarged inversion radius, see Fig.3 in [2].

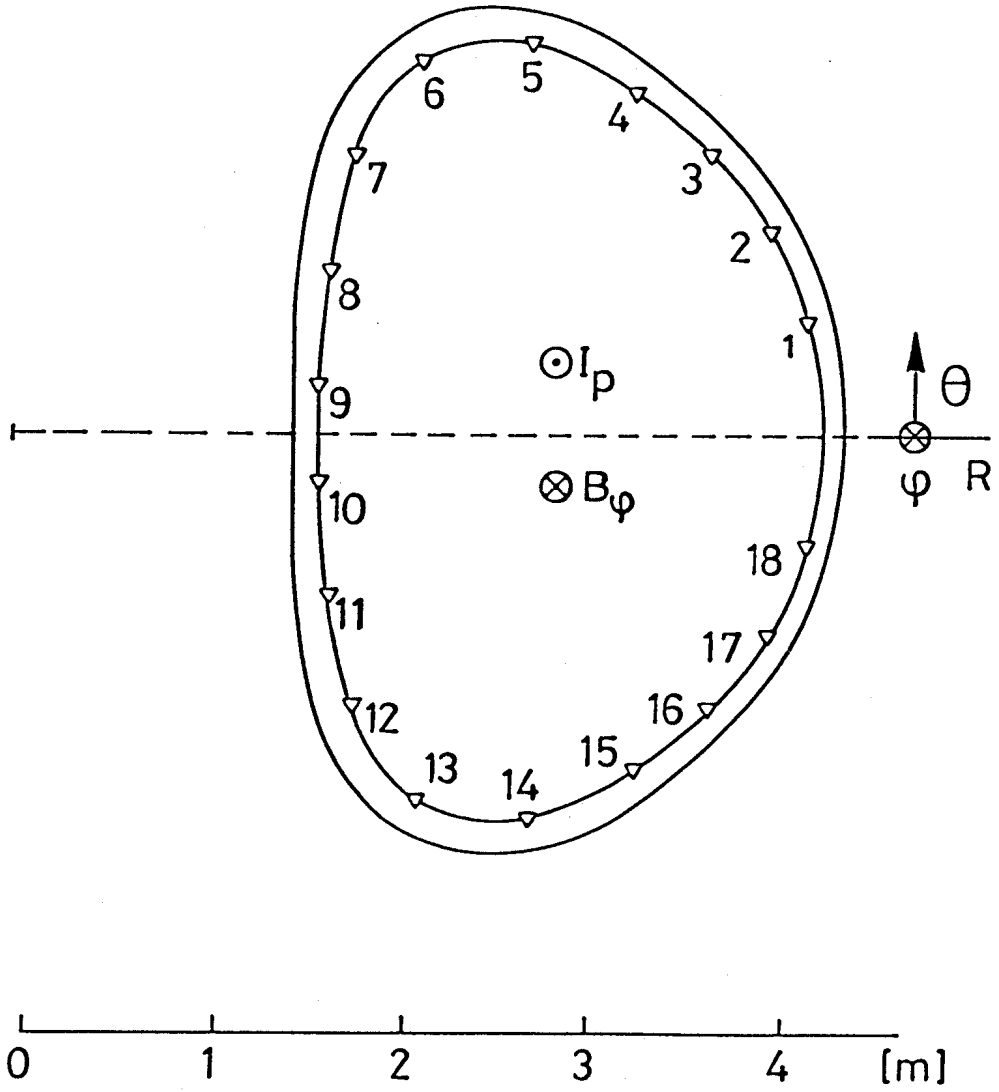

Fig. 1 : Position of the 18 magnetic coils b_θ in an octant of JET. The standard directions of plasma current and toroidal field are indicated.

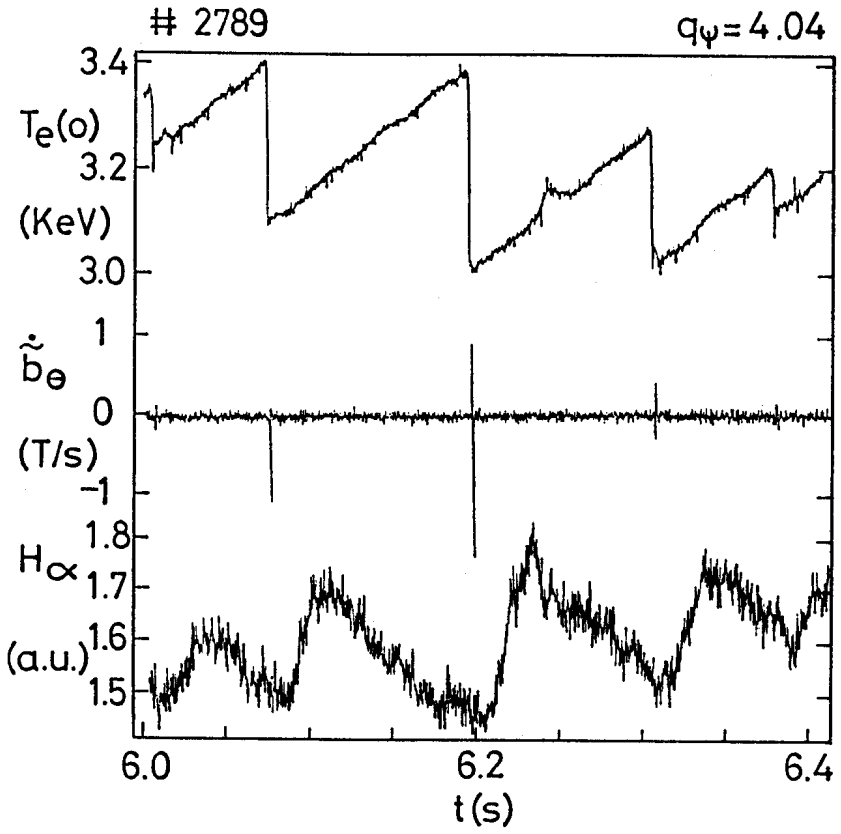

Fig. 2 : Evidence of "spikes" on the magnetic signal correlated with the central temperature collapse of the sawtooth. The maximum of the H_α signal (indicative of the heat pulse reaching the edge) occurs much later.

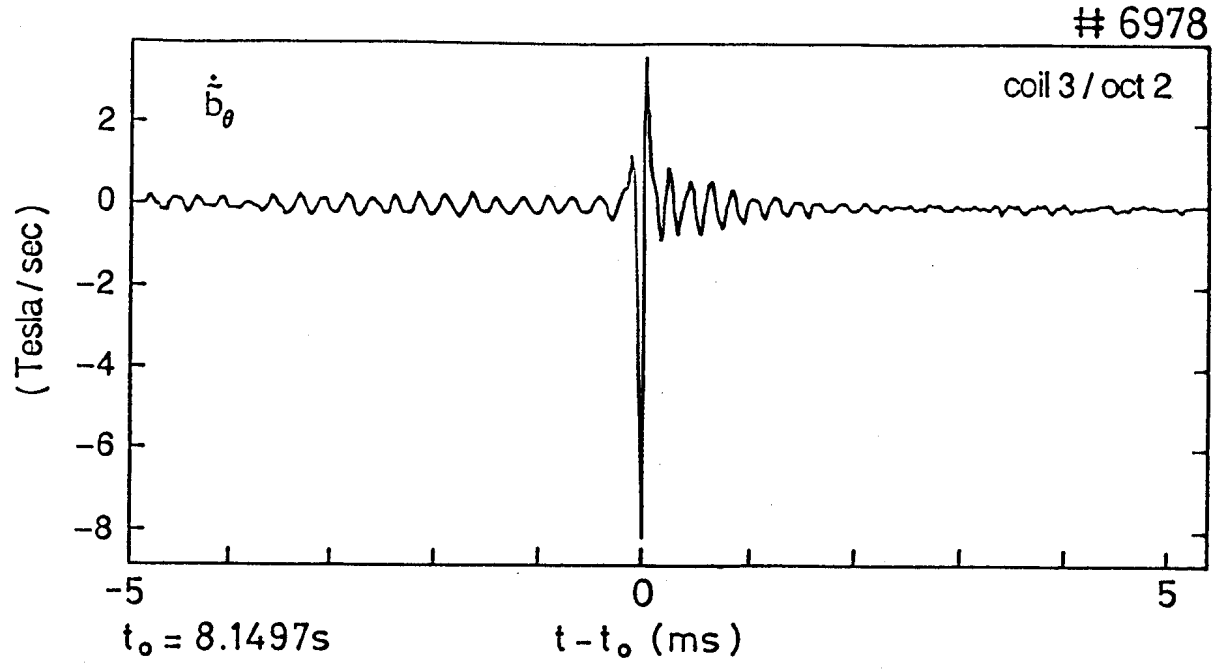

Fig. 3 : Gong occurring during an ongoing Mirnov activity.

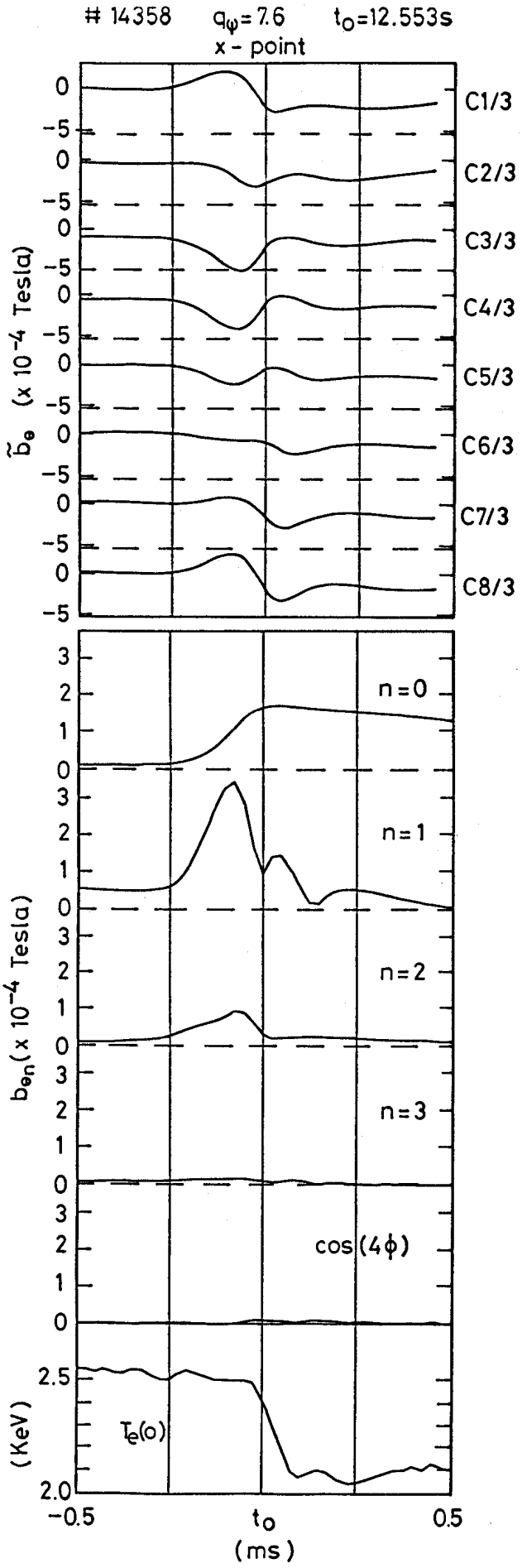

Fig. 4 : Time evolution of the 8 $\tilde{b}_\theta$ (integrated $\tilde{\tilde{b}}_\theta$) and the calculated n=0, 1, 2, 3 and n=4 cosine components. The n=1 component dominates the toroidal spectrum.

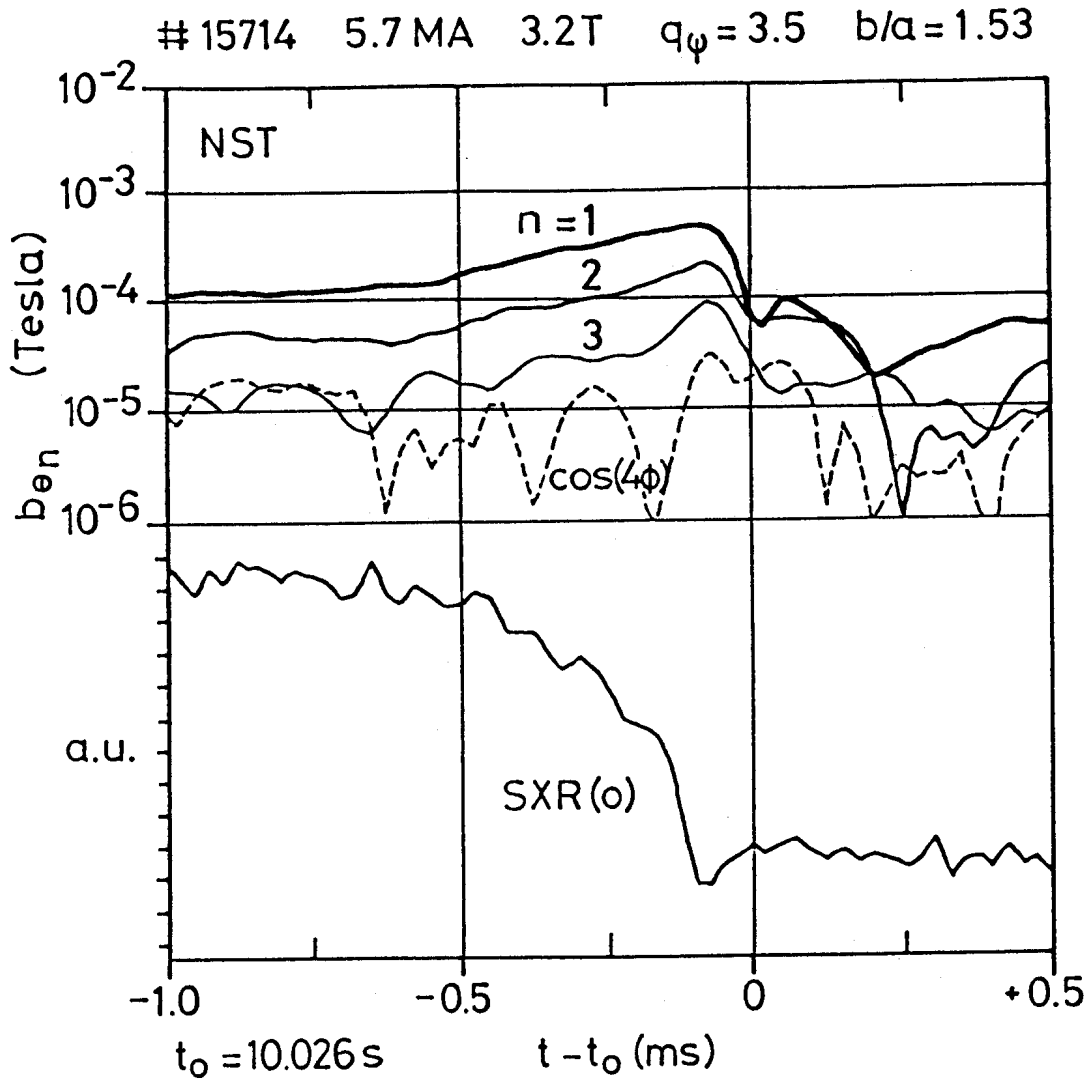

Fig. 5 : Toroidal spectrum of the gong instability for a normal sawtooth (NST).

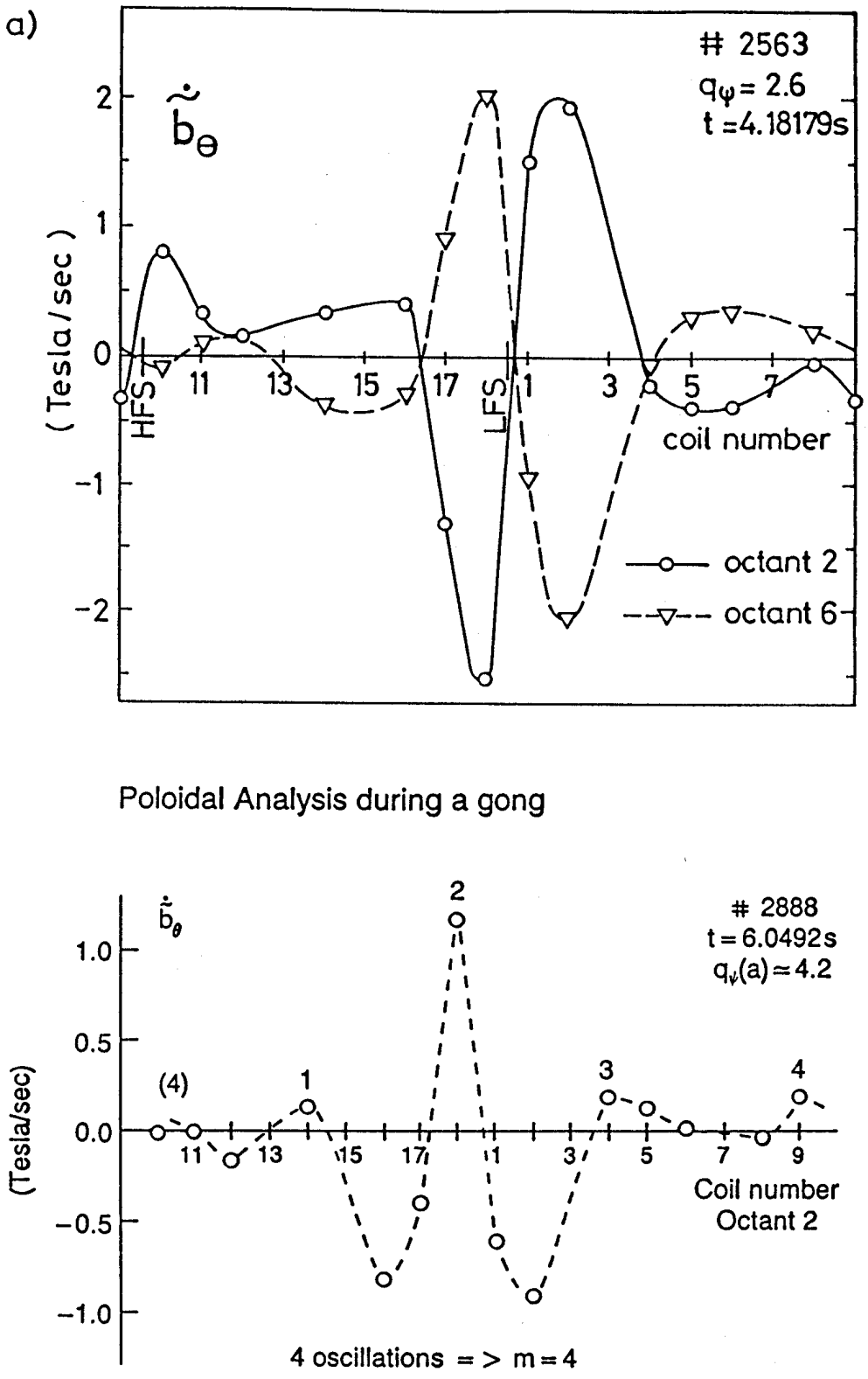

Fig. 6 : Poloidal analysis of the gong ($\tilde{b_\theta}$)
a) Two poloidal arrays located 180° toroidally apart clearly show the dominant n=1 character of the gong, with a remarkable in-out asymmetry. For $q_\psi(a) = 2.6$ the dominant mode appears to be $1<m<3$.
b) For $q_\psi(a) = 4.2$, the dominant mode appears to be m=4.

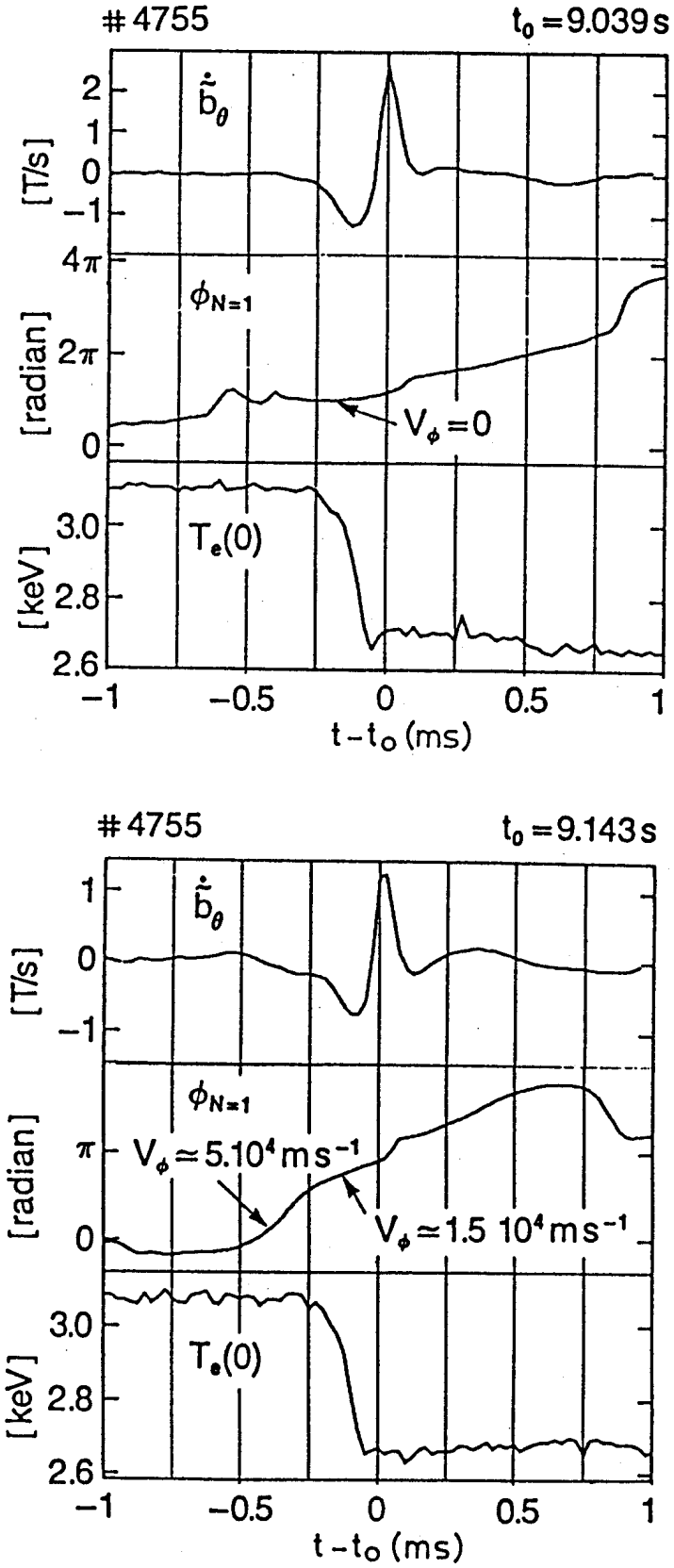

Fig. 7 : Time evolution of n=1 phase showing that the toroidal rotation can be different for two successive gongs belonging to the same discharge.

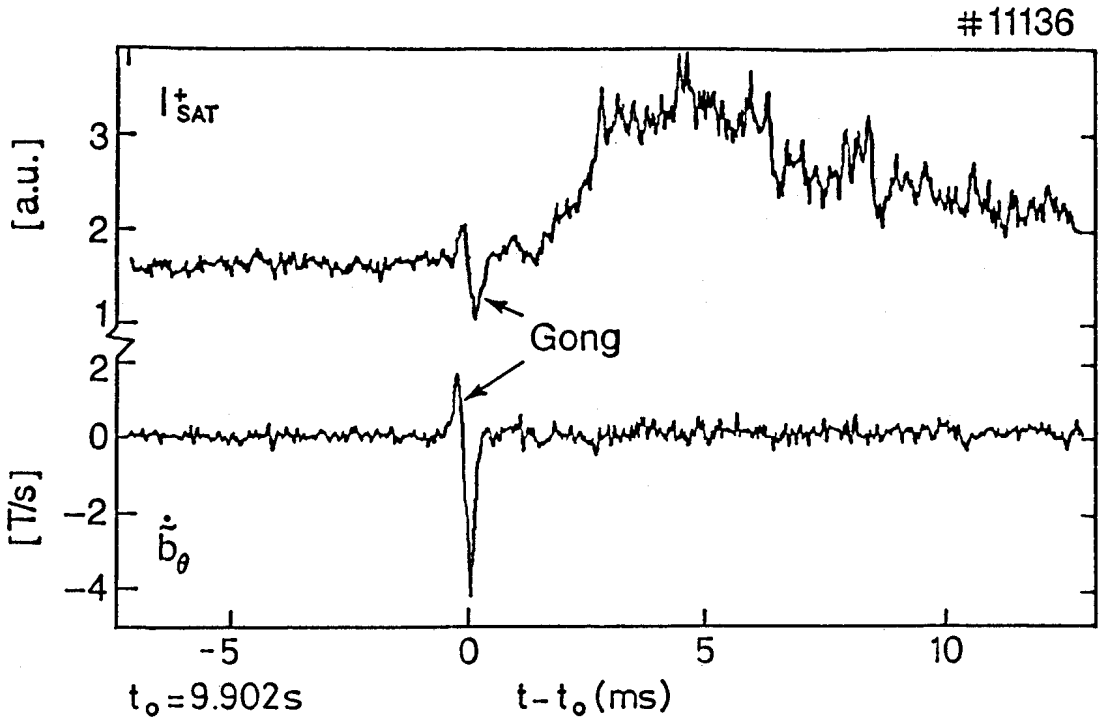

Fig. 8 : The gong can also be observed on an edge Langmuir probe. (The Langmuir probe is located at 4mm from the last closed magnetic surface, on the LFS).

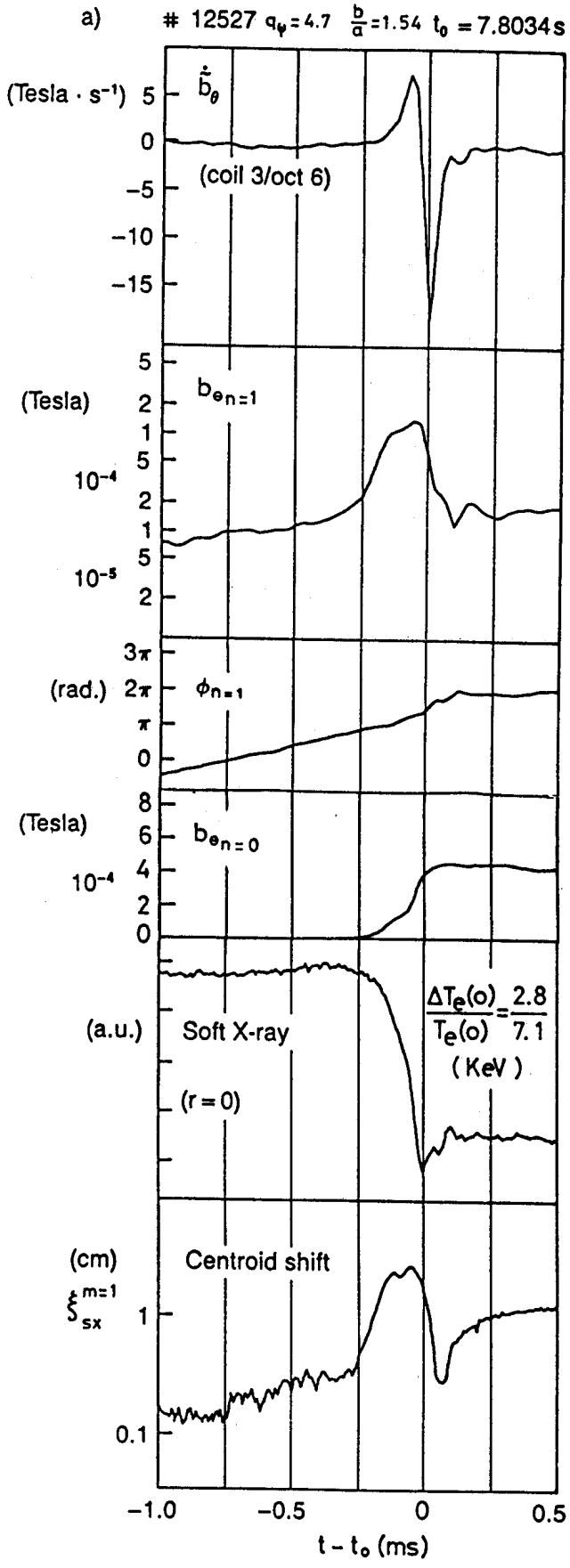
a)
12527 $q_\psi = 4.7$ $\frac{b}{a} = 1.54$ $t_0 = 7.8034$ s
(Tesla · s^{-1})
$\dot{b}_\theta$
(coil 3/oct 6)
(Tesla)
$b_{en=1}$
10^{-4}
10^{-5}
(rad.)
$\phi_{n=1}$
(Tesla)
$b_{en=0}$
10^{-4}
(a.u.)
Soft X-ray
(r = 0)
$\frac{\Delta T_e(o)}{T_e(o)} = \frac{2.8}{7.1}$
(KeV)
(cm)
$\xi_{sx}^{m=1}$
Centroid shift
−1.0
−0.5
0
0.5
t − t_o (ms)

(Fig. 9a)

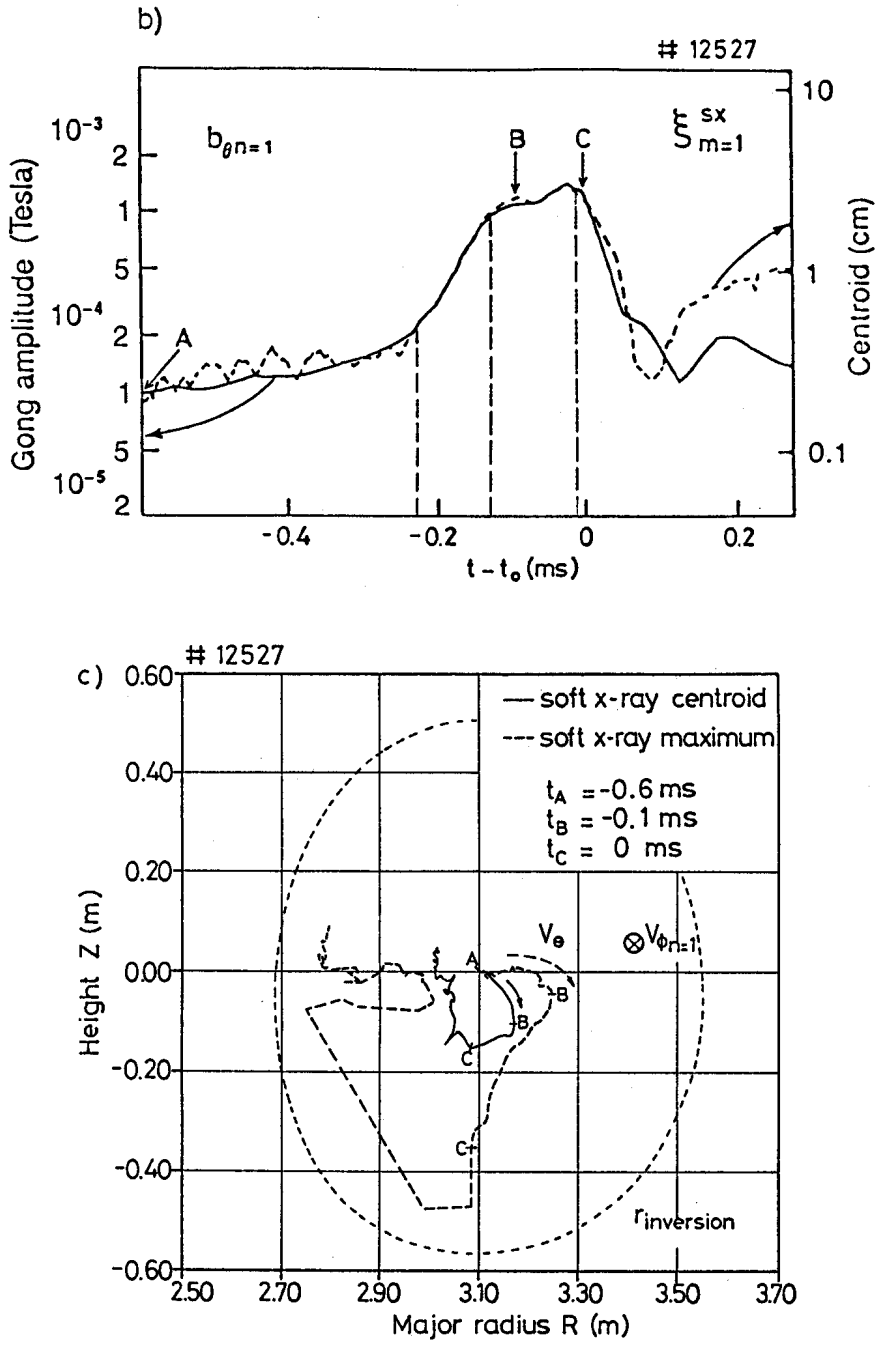

Fig. 9 : Comparison of the gong amplitude and central displacement calculated with the centroid shift, integrated over the full soft X–ray profile.

a) Time evolution of the different traces,

b) Overlapping of the gong amplitude and the centroid shift.

c) Motion of the centroid in the poloidal plane, resulting from integration over $r<r_{inv}$ (full line), and position of the maximum emission (dotted line). The instablity grows between A and B, and saturates between B and C. The helicity of the gong can be deduced from the comparison between the centroid azimuthal motion v_θ (measured with the soft X-rays) and the toroidal gong rotation $v_{\phi\ n=1}$. The resulting direction of the helicity is the same as that of the equilibrium magnetic field.

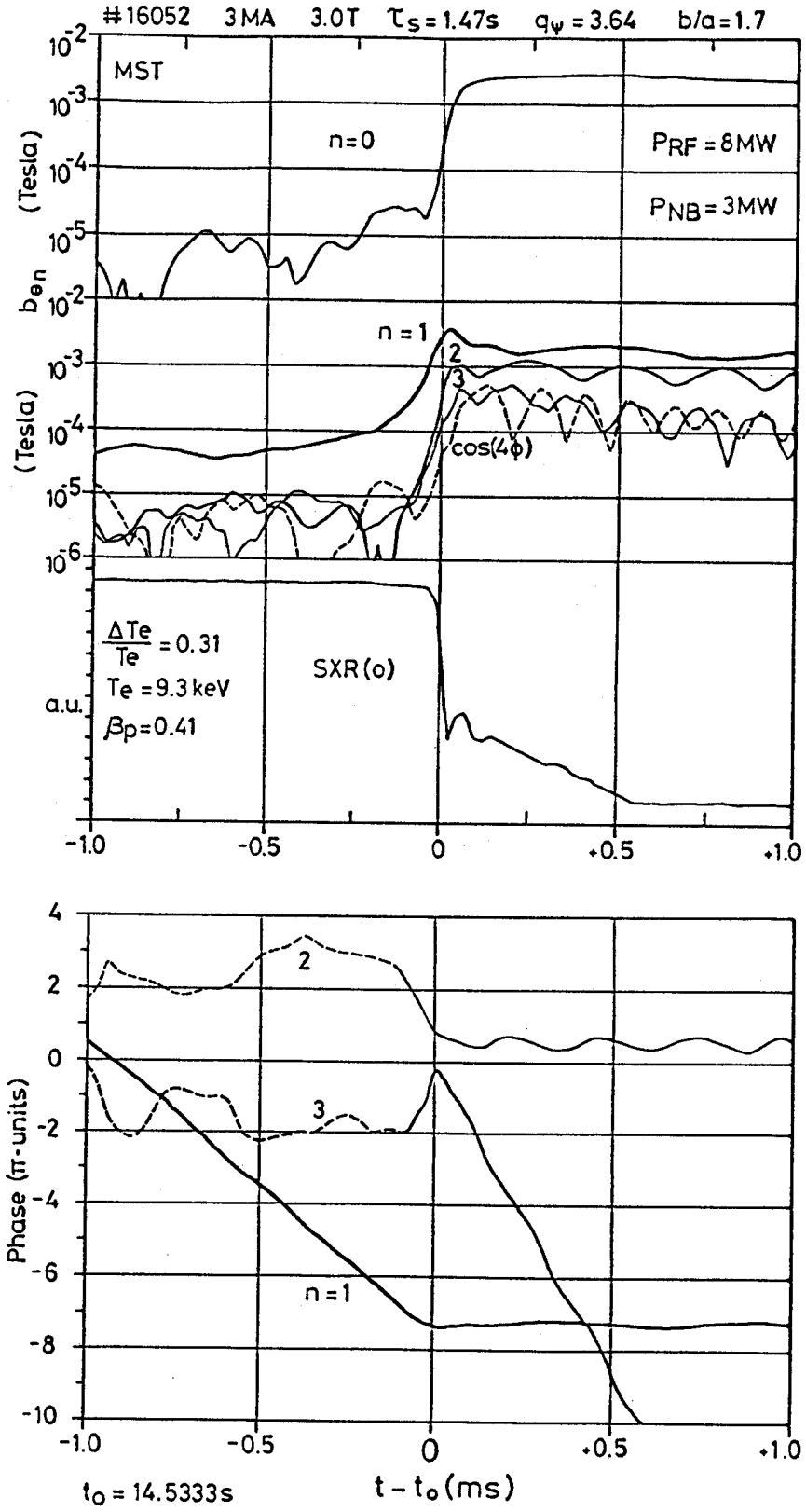

Fig. 10 : Toroidal spectrum of the gong instability for a monster sawtooth (MST). The corresponding phases for the n=1, 2 and 3 modes are also shown in the lower part of the figure.

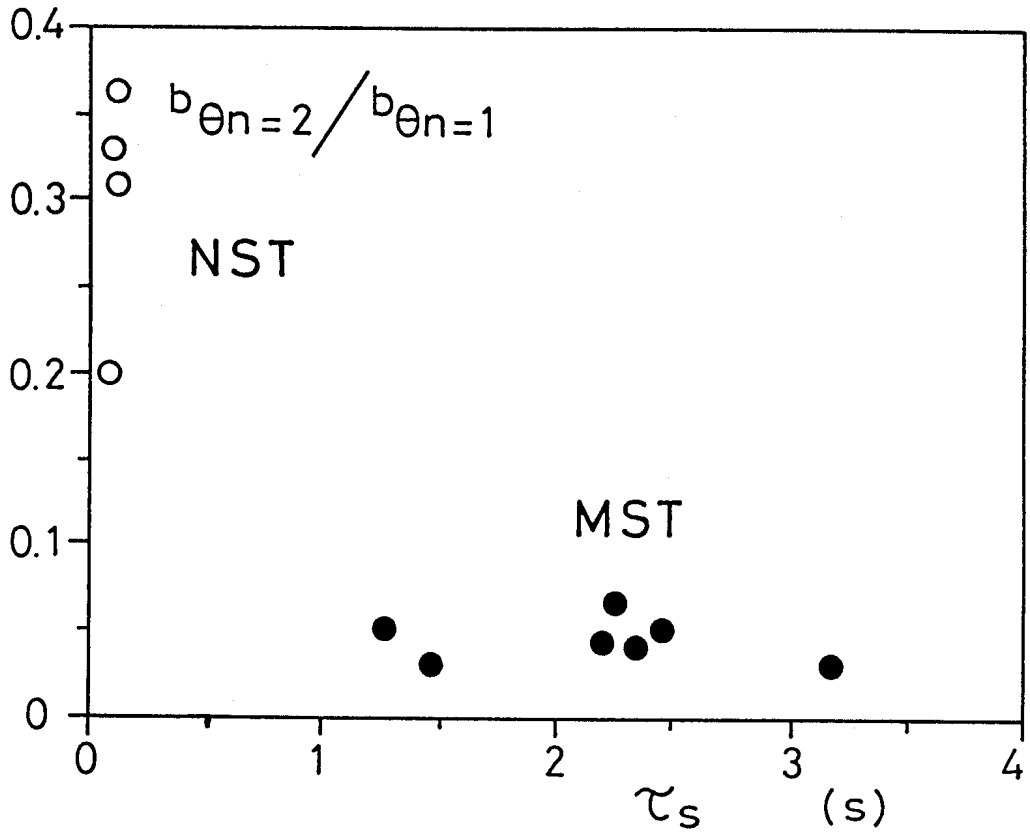

Fig. 11 : Ratio $b_{\theta\, n=2}/b_{\theta\, n=1}$ for NST and MST, depicted as a function of the preceding sawtooth duration.

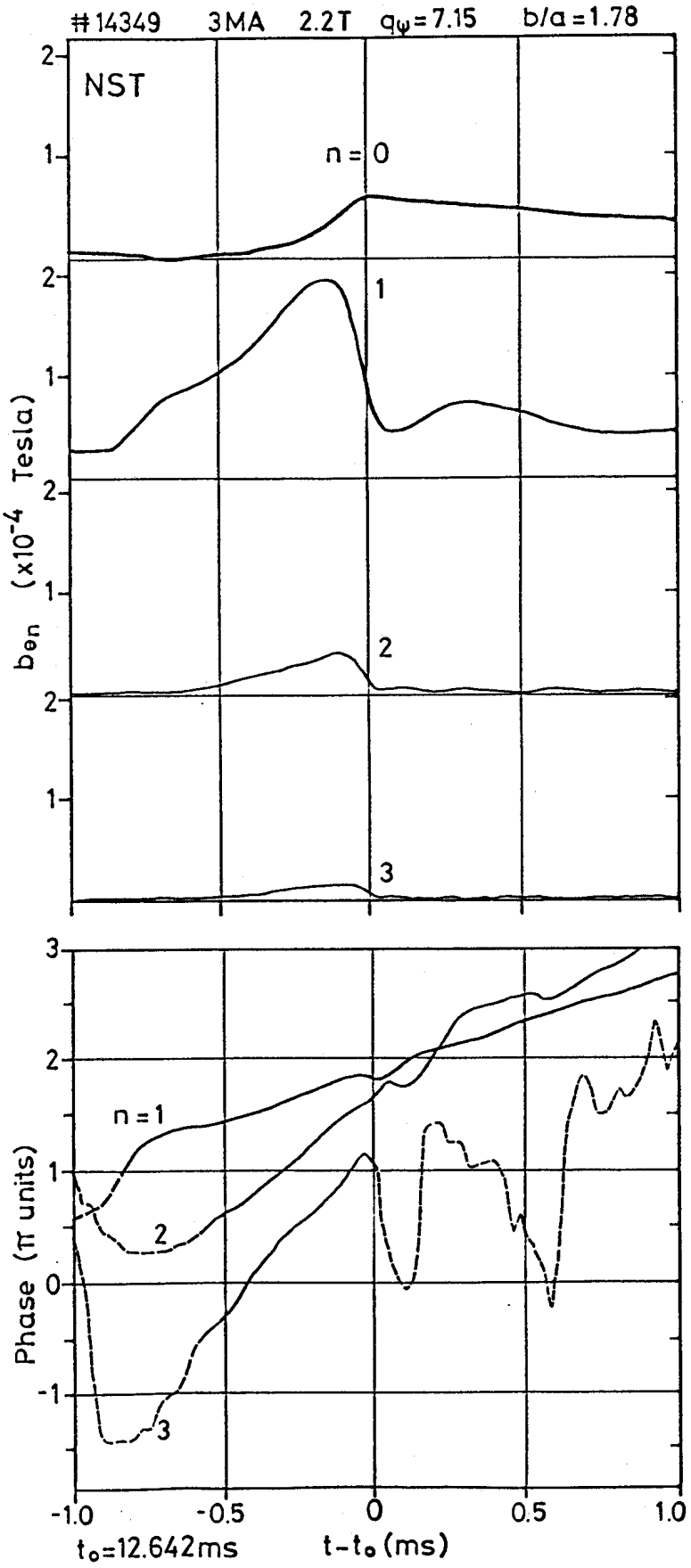

Fig. 12 : Amplitude and toroidal phase for the n=1,2 and 3 components in a NST. The phase plot shows $(\dot{\phi}_{n=1}, \dot{\phi}_{n=2}, \dot{\phi}_{n=3}) \approx (1,2,3)\ \dot{\phi}_{n=1}$ indicative of similar toroidal phase velocities for the different n-components : $v_{\phi\ n} \approx v_{\phi\ n=1}$.

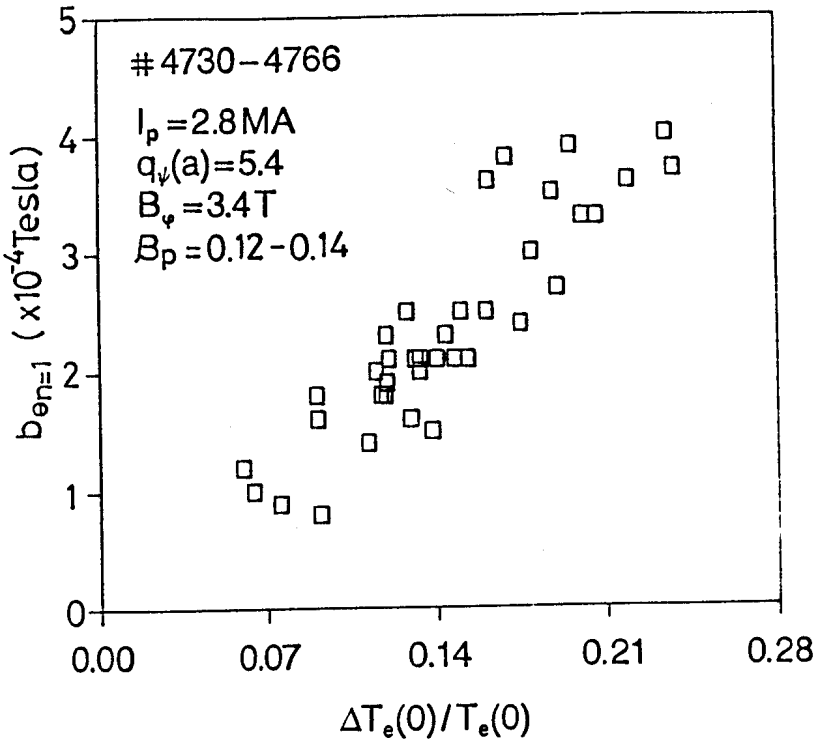

Fig. 13 : Maximum amplitude of $b_{\theta n=1}$ (at saturation of the instability) for normal sawteeth versus the normalized central temperature drop $\Delta T_e(0)/T_e(0)$.

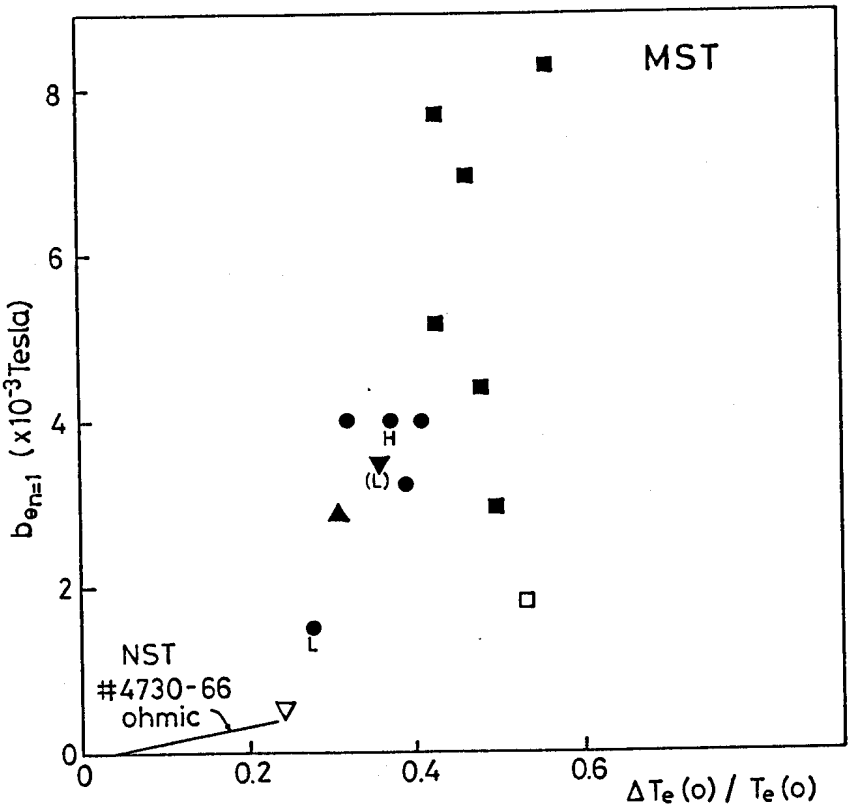

Fig. 14 : Maximum amplitude of $b_{\theta n=1}$ for monster sawteeth versus $\Delta T_e(0)/T_e(0)$. The trend for normal sawteeth is indicated in the left lower corner. Different series of monster sawteeth are indicated by different symbols, see Table I.

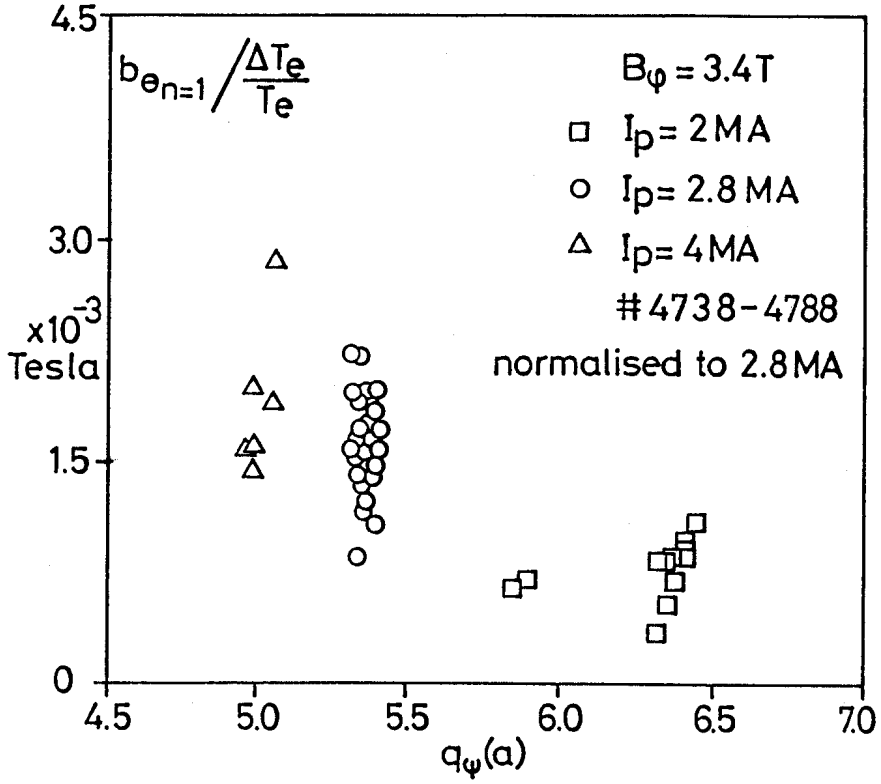

Fig. 15 : The gong amplitude $b_{\theta n=1}$ shown here for normal sawteeth is smaller for larger $q_\psi(a)$. The gong amplitude is both normalized to the relative temperature crash $\Delta T_e(0)/T_e(0)$ and to a plasma current of 2.8 MA (multiplication by 2.8 M/Ip).

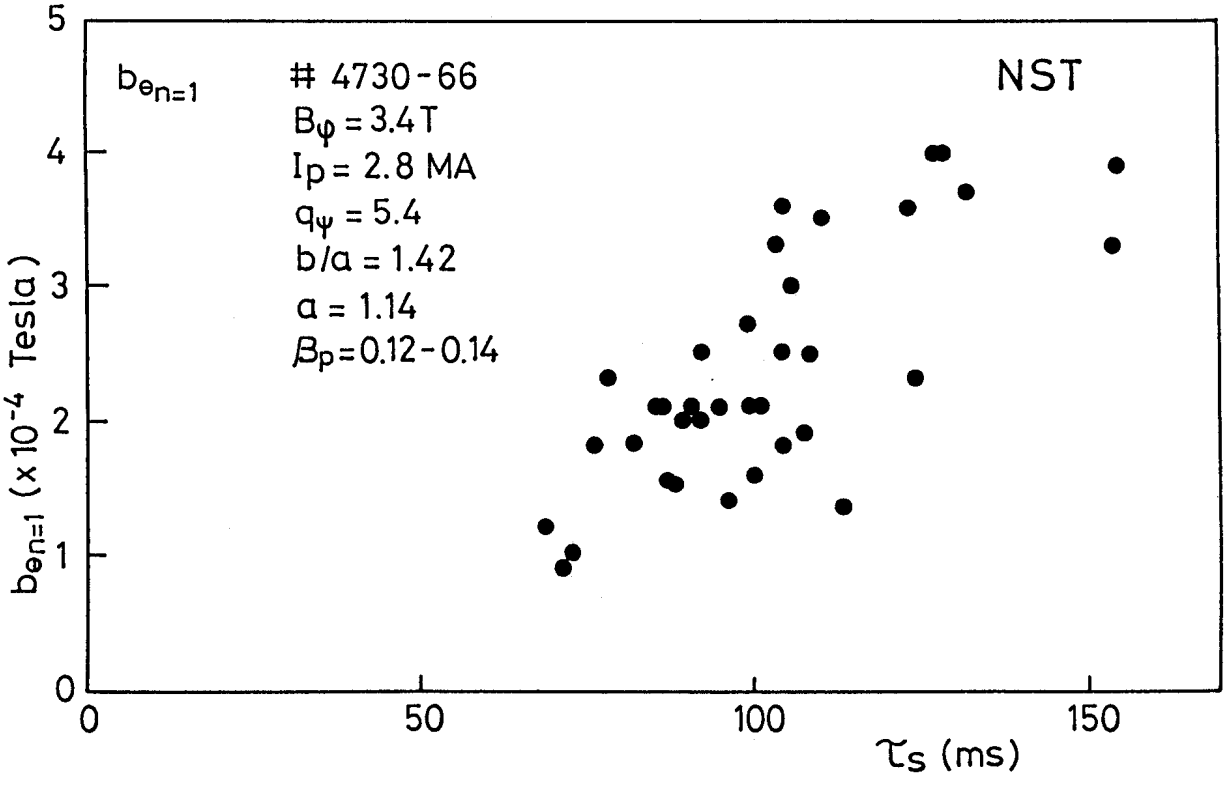

Fig. 16 : The gong amplitude $b_{\theta n=1}$ increases with sawtooth period τ_s for normal sawteeth.

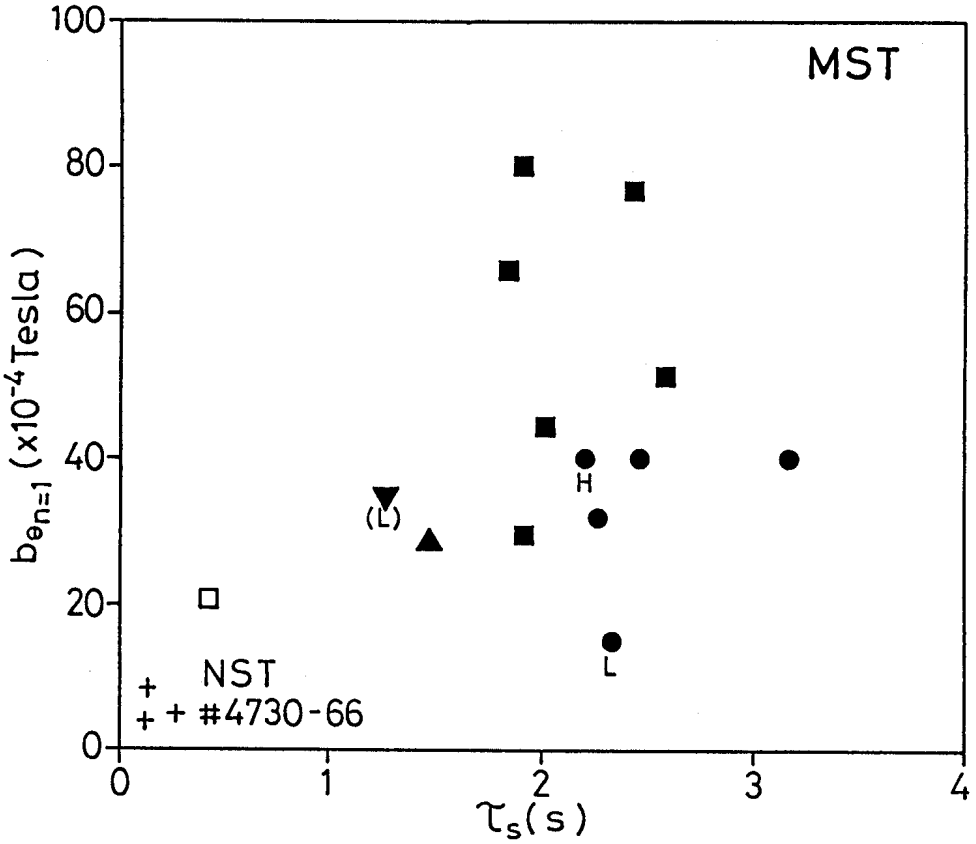

Fig. 17 : The gong amplitude $b_{\theta n=1}$ for monster sawteeth is somewhat below the extrapolated value for normal sawteeth (lower left corner) for increasing sawtooth period τ_s. Same data as in Fig. 14, see Table I.

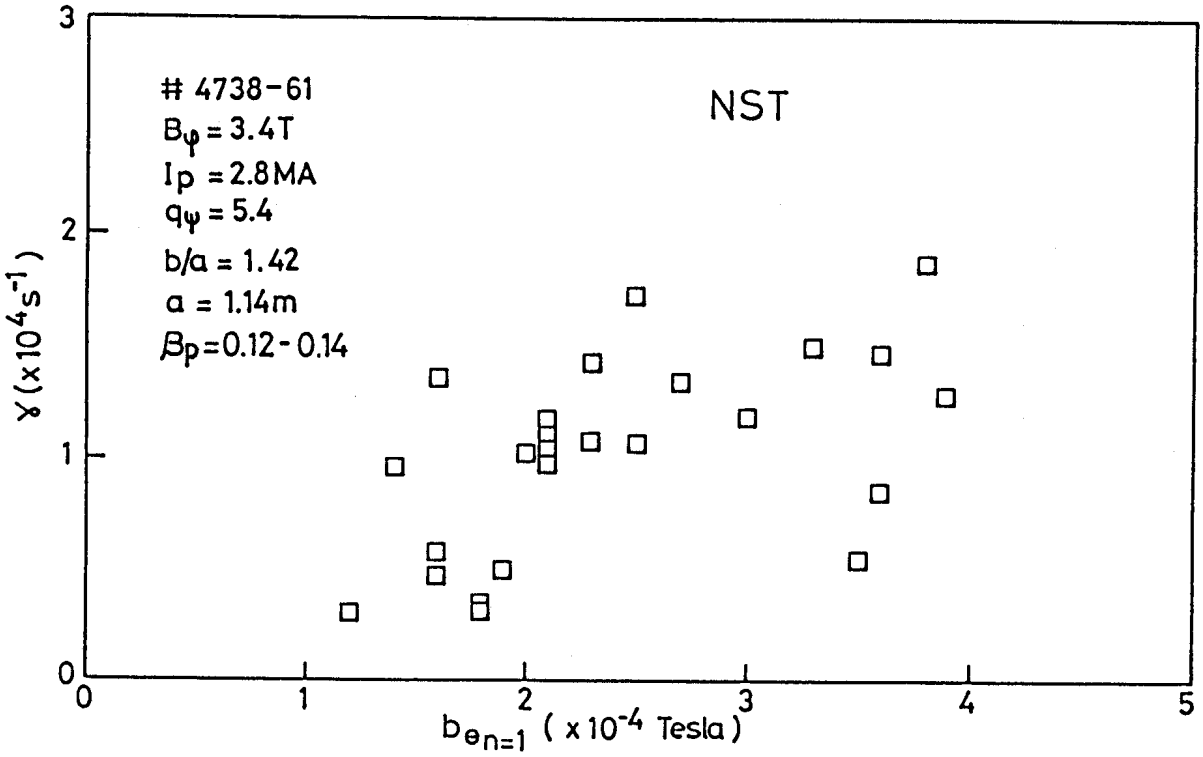

Fig. 18 : Growth rate of the instability versus $b_{\theta n=1}$ for normal sawteeth.

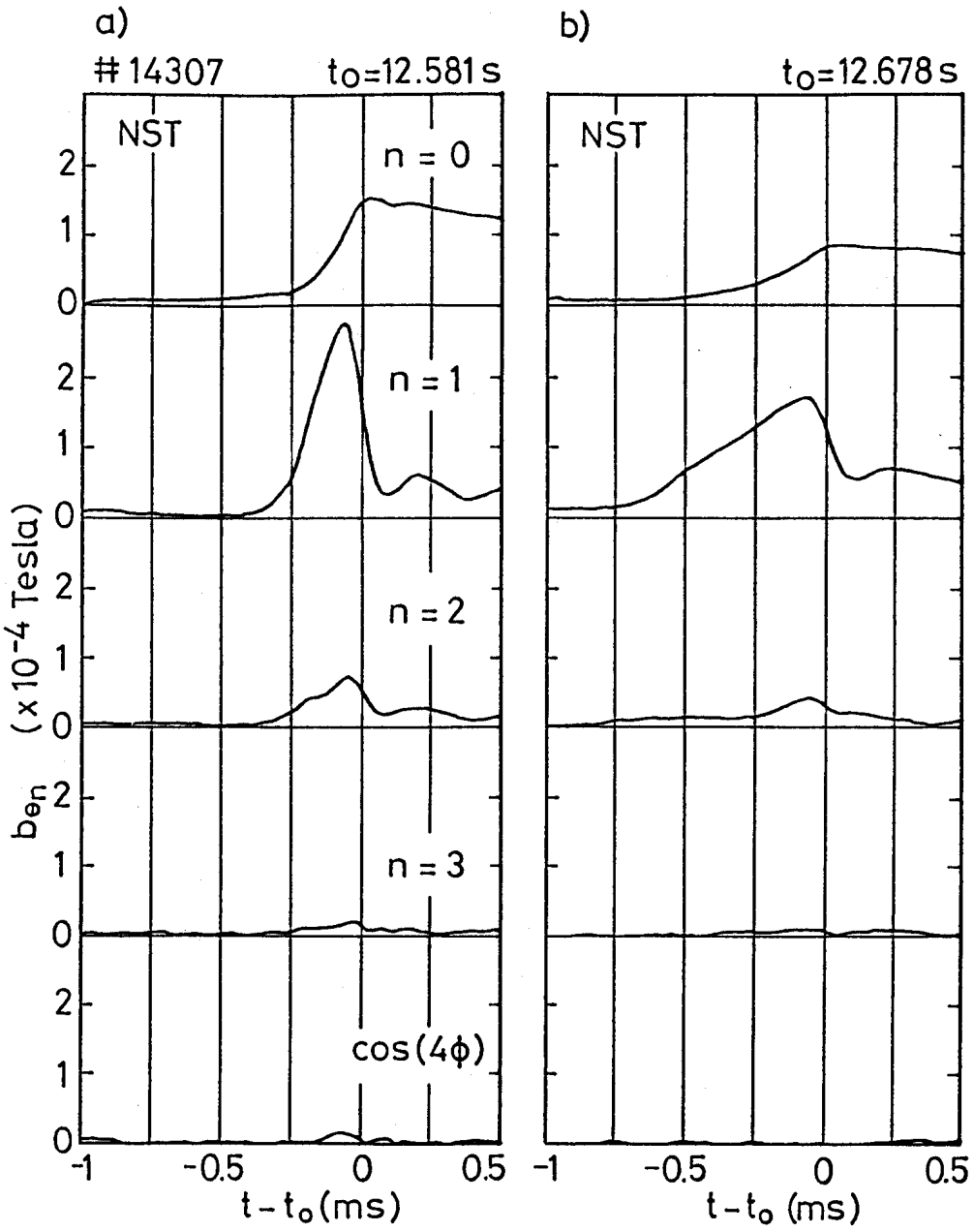

Fig. 19 : Two consecutive sawteeth can show growth rates varying by more than half an order of magnitude in normal sawteeth. The growth rate does not depend on the sawtooth duration which is a) τ_s = 104 and b) 97 ms. The amplitude of the gong varies as a) $\Delta T_e/T_e$ = 0.18 and b) 0.10.

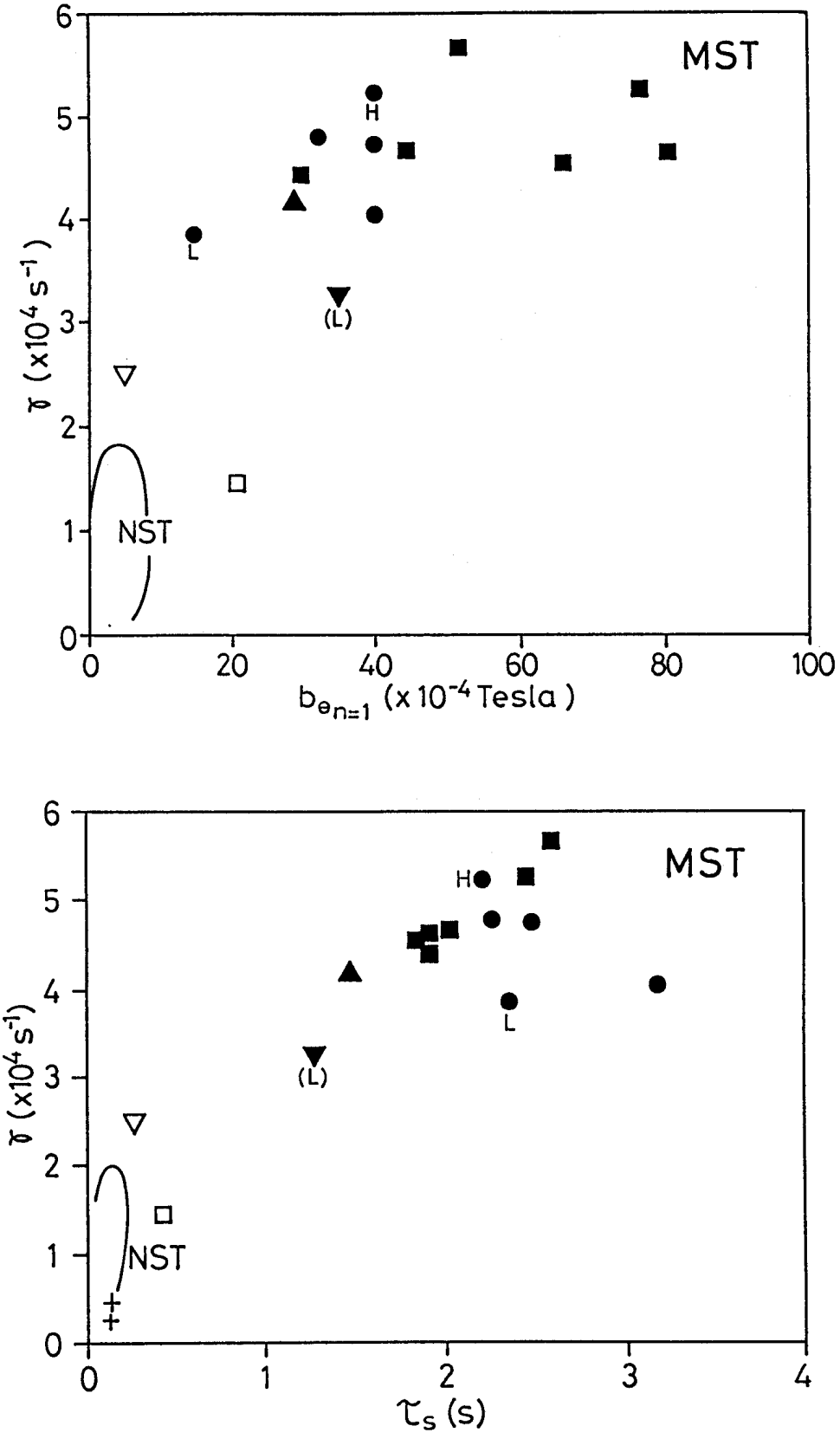

Fig. 20 : a) Growth rate of the instability versus the $b_{\theta n=1}$ component for monster sawteeth.
b) Growth rate versus sawtooth period τ_s. Same data as in Figs. 14 and 17, see Table I.
The trends for normal sawteeth are indicated in the lower left corners.